



Structural robustness evaluation of steel frame buildings with different composite slabs using reduced-order modeling strategies

Junjie Wang^a, Ke Ke^{b,c,*}, Wei Wang^d

^a Department of Building and Real Estate, Hong Kong Polytechnic University, Hong Kong, China

^b School of Civil Engineering, Chongqing University, Chongqing, China

^c Key Laboratory of New Technology for Construction of Cities in Mountain Area (Ministry of Education), Chongqing University, Chongqing, China

^d Department of Structural Engineering, Tongji University, Shanghai, China

ARTICLE INFO

Keywords:

Composite slab
Steel frame
Robustness
Disproportionate collapse
Progressive collapse

ABSTRACT

This study presented reduced-order modeling methods for evaluating the structural robustness of steel frame buildings with different composite floor slabs under ground floor column loss scenarios. The adequacy of the reduced-order modeling technique was justified by relatively high-fidelity models, which were verified by a full-scale composite floor test and detailed material coupon tests. This reduced-order modeling method was applied to the progressive collapse simulation of a five-story prototype building. The effect of floor slabs, slab rebars, and steel decks' longitudinal continuity on its progressive collapse resistance was examined. Composite slabs with four different profiled steel decks were considered in this study, which are trapezoidal deck, dovetail deck, reentrant deck, and rebar-truss deck; in addition, reinforced concrete (RC) slab was also considered for comparative purposes. To account for the possible sudden column failure scenario in practice, an energy-based approach was used to convert the quasi-static response curves to dynamic response curves. The structural robustness was evaluated by comparing each column failure case's dynamic ultimate capacities with corresponding design requirements. The structural robustness of prototype buildings under progressive collapse scenarios was summarized and discussed. The analysis results showed that the structural robustness of the prototype building with rebar-truss composite slab was higher than that with RC slab or other composite slabs. The prototype building with floor slabs using HRB400 rebars had higher structural robustness than that using CRB550 rebars.

1. Introduction

The disproportionate collapse (or progressive collapse) of buildings caused by local structural component failure attracted great attention in the civil engineering community after the bombing of the Alfred P. Murrah Federal Building in 1995 and the terrorist attack on the World Trade Center in 2001. When disproportionate collapse of buildings occurs, the initial local structural component failure can successively spread to the surrounding structural components, eventually resulting in the collapse of an entire structure or a disproportionately large part of it [1]. The structural resistance against disproportionate collapse, or, to speak more correctly, the insensitivity of a structure to local failure, can be expressed by the term “structural robustness” [1,2]. Several current guidelines [3–5] have emphasized that building structures must have sufficient structural robustness to reduce the potential risk of the

structural disproportionate collapse. The structural robustness of buildings can be improved by providing alternative load paths to prevent the spread of the local damage induced by critical structural element failure [1,6,7]. For the steel frame buildings, the common mechanisms conducive to the development of alternative load paths include: i) beam mechanism [8]; ii) catenary action of beams and tensile membrane action of slabs [6]; iii) Vierendeel mechanism above the damaged column [8], iv) support provided by infilled walls, braces, and roof trusses [9–11].

The significant contribution of the floor slabs to the structural robustness of steel frame structures has been verified by experimental or numerical studies from different perspectives [11–26], and the studied floor slabs can be roughly classified into two categories: RC slabs [16,19,23,24] and composite slabs [11–15,17,18,20–22,25–28]. Composite slabs typically consist of profiled steel decks and concrete slab

* Corresponding author at: School of Civil Engineering, Chongqing University, Chongqing, China.

E-mail address: ke.ke@cqu.edu.cn (K. Ke).

<https://doi.org/10.1016/j.jcsr.2022.107371>

Received 15 February 2022; Received in revised form 11 May 2022; Accepted 6 June 2022

Available online 17 June 2022

0143-974X/© 2022 Elsevier Ltd. All rights reserved.

topping. Compared with RC slabs, temporary slab formworks and floor supports are not needed for the composite slabs, as the profiled steel decks are usually designed as permanent formworks to resist the wet concrete weight and the construction loading. Thus, the composite slabs are widely adopted in modern steel frame buildings to expedite construction speed and save labor costs. To date, for the structural robustness research related to the composite slabs, three widely used types of composite slabs are studied, including trapezoidal composite slabs [11–15,18,20,22,25,27,28], dovetail or reentrant composite slabs [17,21,22,26] (Fig.1). However, most of these studies focus on only one type of composite slab, and few studies compare the differences between different composite slabs in improving the structural robustness of steel frame structures.

To investigate the slab effect on the structural robustness of steel frame buildings, the full structural level experimental testing would be more accurate than the substructure level testing [29]. However, limited by the complexity and extraordinarily high cost of full structural system testing [30,31], most of the experimental studies on the structural robustness of steel frame structures with floor slabs fall into the connection level [16,17,19,22,32] and single-story substructure level [18,20,21,23,25,26,33–35]. In view of this, numerical analysis is a relatively feasible approach when analyzing the structural robustness of an entire steel frame building. In this context, a full three-dimensional analysis as the most rigorous way to strictly investigate the structural robustness of a building is generally required since planar analysis may not always be reliable for the progressive collapse simulation [14]. However, the entire steel frame building analysis based on high-fidelity models may be time-consuming and can lead to high computational costs. For this reason, reduced-order models were usually developed to replace high-fidelity models to maintain computational effectiveness [11,14,15,27,36–39]. Nevertheless, in a reduced-order model, it is challenging to reflect the influence of the local stress state fully (e.g., stress triaxiality and Lode angle) on the steel fracture at the connection region, which is critical from the perspective of an accurate progressive collapse simulation of steel structures [11,40].

To fill the aforementioned research gaps, a 5-story steel frame prototype building was designed, and the structural robustness of the prototype building with different floor slabs was evaluated and compared using a finely calibrated reduced-order modeling approach. Fig. 2 outlines the modeling methodology of the reduced-order modeling approach. Based on the test results of a full-scale single-floor composite floor substructure test and corresponding material coupon tests, high-fidelity models were established and validated [40]. Then, the reduced-order models of the connections and floor slabs in the prototype building were calibrated by the corresponding high-fidelity models.

Afterward, the influences of different floor slabs, different slab rebars, and the steel decks' longitudinal continuity on the structural robustness of the prototype building were investigated using the calibrated reduced-order models. All the numerical models and simulations in this study were performed using the LS-DYNA program.

2. Prototype building

As shown in Fig. 3a, a five-story, 5×5 -bay prototype steel moment-resisting frame building was designed according to Chinese codes [41–45]. The design basic earthquake acceleration was 0.05 g (gravitational acceleration). The design dead load (DL) and live load (LL) were 5 kN/m^2 and 2 kN/m^2 , respectively. The story height of the prototype building was 4.5 m, with the span length of the girder and beam being 9 m and 6 m, respectively. As shown in Fig. 3b, the girder-to-column connection and beam-to-column connection were welded flange-bolted web connections, while the beam-to-girder connection was bolted shear tab connection. H-shaped steel sections $\text{H}500 \times 200 \times 10 \times 16$ and $\text{H}300 \times 150 \times 6.5 \times 9$ were used for girders and beams, respectively. Square steel tube $\square 400 \times 400 \times 12$ was used for columns. Grade 10.9 M24 high strength bolts were used in the girder-to-column connection, whereas Grade 10.9 M20 high strength bolts were used in the beam-to-column connection and beam-to-girder connection. High-strength bolts were used to avoid the shear failure of the bolt shanks, which is a brittle failure mode compared to the bolt hole failure. The detailed information about the connections is given in Fig. 3b.

A total of five types of floor slabs were considered for the prototype building, including RC slab and four types of composite slabs, as shown in Fig. 3c. Except for the above-mentioned trapezoidal, dovetail, and reentrant composite slabs, a relatively new type of composite slab, rebar-truss composite slab [46,47], was also considered. As illustrated in Fig. 1d, the rebar-truss steel deck has two parts: rebar-trusses and profiled steel decks. Each rebar-truss has three parts: one top chord, two bottom chords, and two curled web bars. The factory-welded rebar-trusses greatly reduce the on-site rebar tying work and effectively ensure the construction quality of the concrete cover thickness and the rebar spacing. The rebar-trusses are welded to the ribs of the profiled steel decks in the factory. Since the freshly casted concrete has no strength initially, the RC slabs should be temporarily supported by the shoring system during construction. Hence, the construction loading was not considered in the design of the RC slabs. For the construction of the composite slabs, the slab shoring system should be avoided whenever possible because it reduces the construction speed, affects the construction sequence, and increase labor and cost [48]. Hence, the construction loading was considered in the design of the composite slabs.

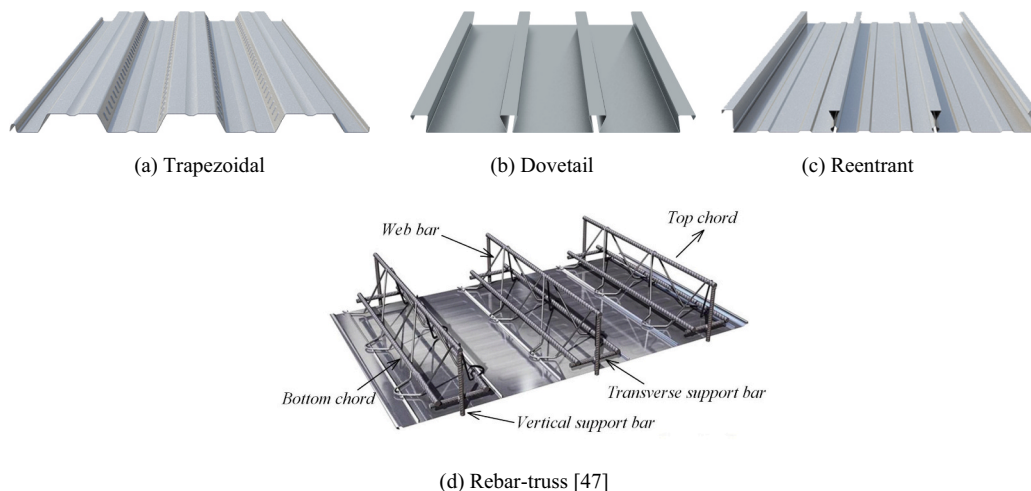


Fig. 1. Typical geometric shapes of profiled steel decks.

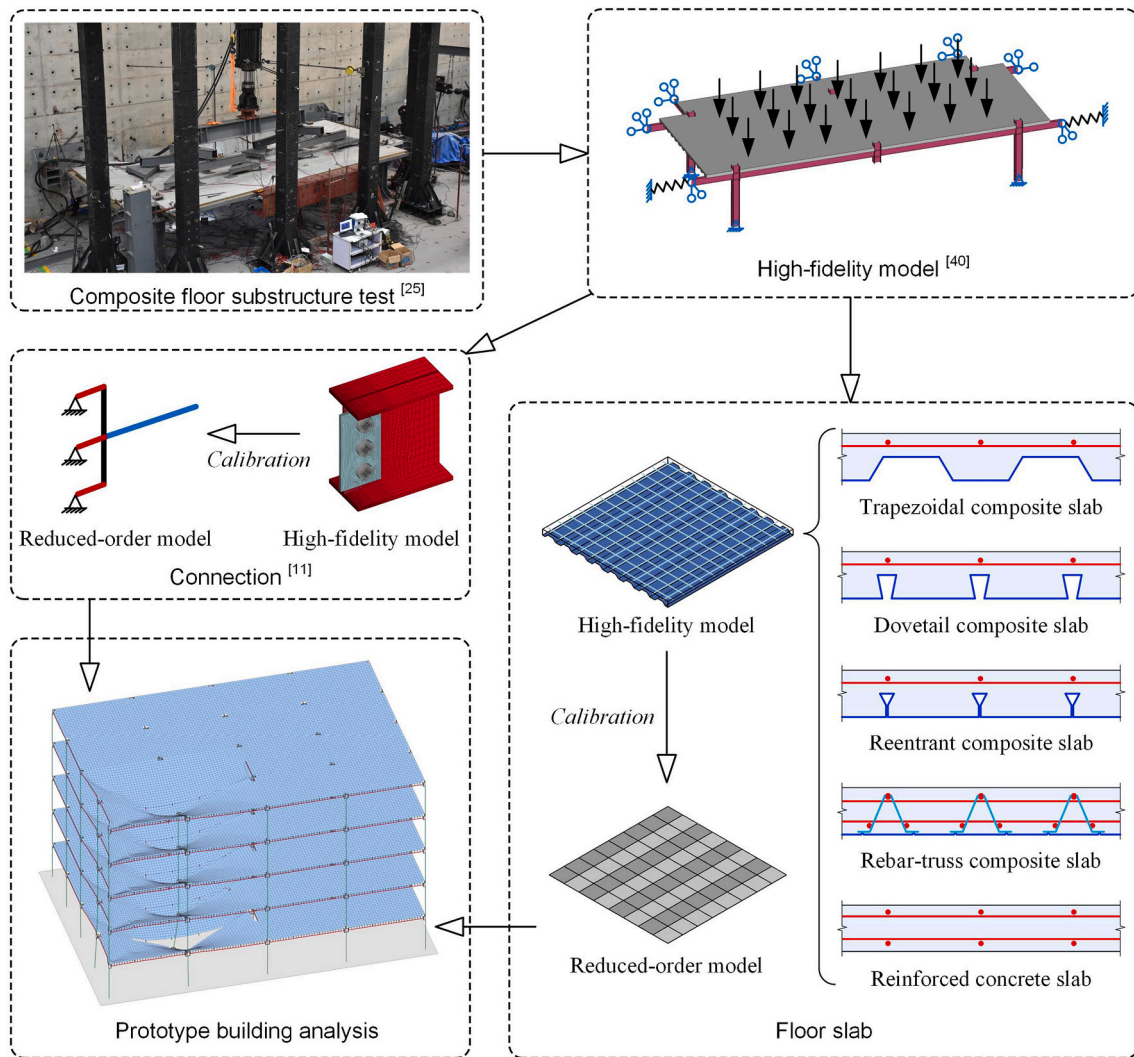


Fig. 2. Flowchart of the reduced-order modeling approach.

The profiled steel decks were designed to support the construction loads and the weight of the wet concrete, and the allowable unshored clear spans of the profiled steel decks were designed to exceed the beam spacing (i.e., 3 m).

The details of the designed floor slabs are shown in Fig. 3c, and these slabs all had a cross-sectional height of 100 mm. For the trapezoidal, dovetail, and reentrant composite slabs, and RC slab, welded rebar meshes with Φ 8 ribbed bars were selected, and bar spacing was 200 mm in both directions. For the rebar-truss composite slab, the top chords, bottom chords, and web bars were Φ 10 ribbed bars, Φ 8 ribbed bars, and Φ 4.5 round bars, respectively, while the transverse bars were Φ 8 ribbed bars with a spacing of 200 mm. The rebar-truss spacing was 200 mm. The concrete cover for these slabs was 15 mm thick. The thickness of all the steel decks was 1.2 mm. The longitudinal direction of profiled steel decks was parallel to the girder axis. The length of each profiled steel deck was 9 m. As shown in Fig. 3d, at the longitudinal ends of the profiled steel decks, they were restrained to the beam top flanges by the shear studs. In the transverse direction, these decks were mechanically clasped by the curled edges. 19 mm diameter shear studs were used to restrain the floor slabs to the top flanges of the girders and beams. To obtain full shear connections, the shear stud quantities installed on each girder and beam were 85 and 38, respectively.

The structural steel used for all columns, girders, beams, and steel decks was Q345 steel. Note that rebars used in the floor slabs generally included cold-rolled ribbed bars (CRB) and hot-rolled ribbed bars (HRB).

Hence, both types of bars were used in the prototype building to examine their effects on the structural performance, and the selected bar grades were CRB550 and HRB400, respectively. The shear studs were selected according to the code GB/T 10433 [49], and the lower limits of their yield strength, tensile strength, and elongation were 320 MPa, 400 MPa, and 0.14, respectively. The strength grade of concrete was C30.

3. High-fidelity models of composite slabs and verifications

3.1. Modeling methods

As mentioned in Section 1 (Fig. 2), the high-fidelity models of floor slabs are developed in this section, which will be used as the benchmark to calibrate the reduced-order slab models later. An overview of high-fidelity models of various composite slabs is given in Fig. 4, and five types of floor slabs were built based on a 2.4×2.4 m square slab extracted from the prototype building described above.

As shown in Fig. 4, the high-fidelity slab models were simulated under the tensile-bending loading state. According to the available experimental studies [16–23,25,26,32,33], under the column removal scenarios, the floor slabs in the steel frame structures are mainly failed by the combined force of bending and in-plane tension, while no significant contribution from the out-of-plane shear (punching shear) and in-plane shear failure modes have been observed. Hence, the tensile-bending loading state was adopted as the benchmark loading state for

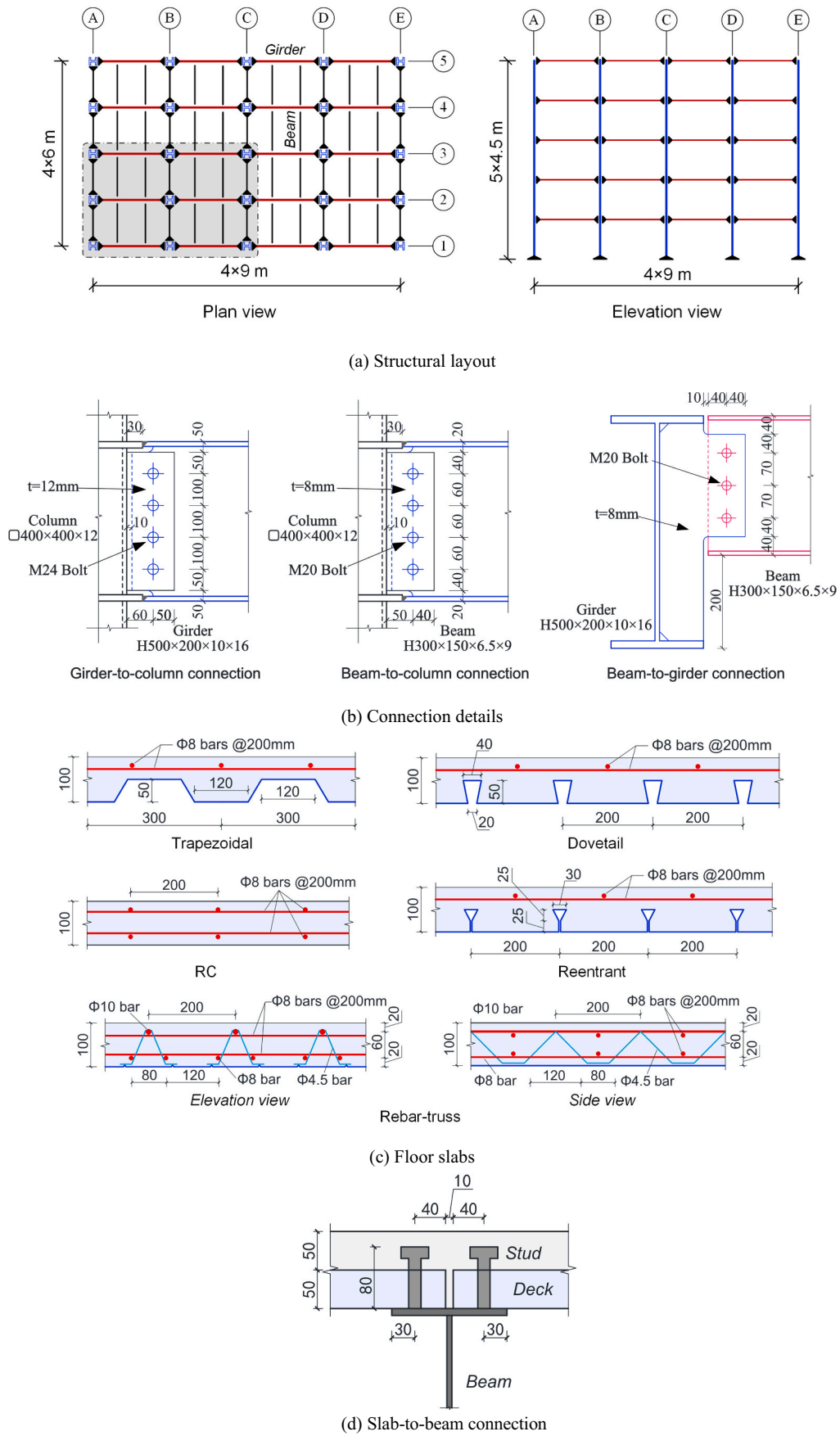


Fig. 3. Prototype building.

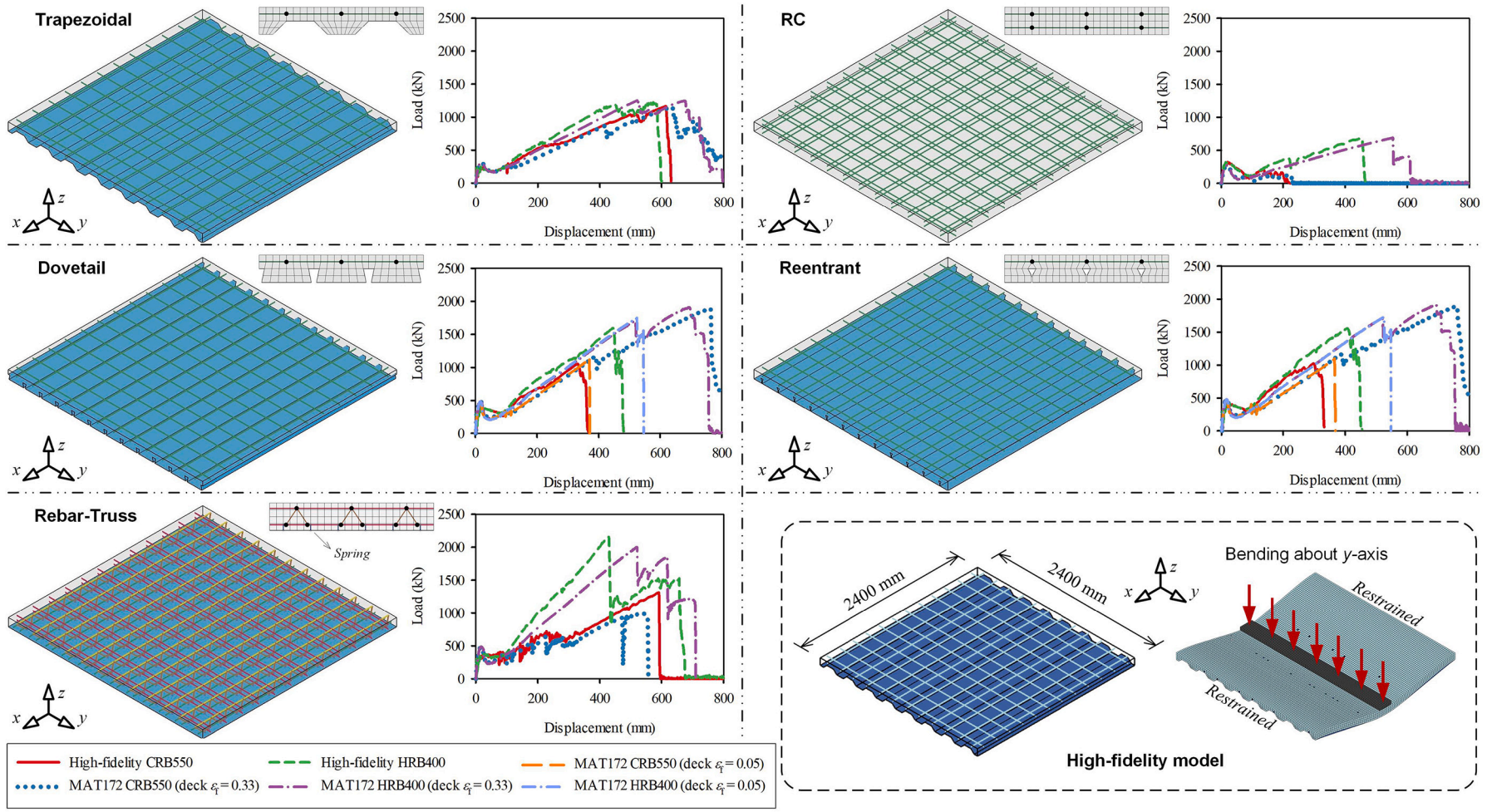


Fig. 4. High-fidelity modeling of composite slabs.

calibrating the slab models. As shown in Fig. 4, to facilitate the calibration of the reduced-order models in Section 4, the tensile-bending loading state was achieved by fully restraining the slab's two parallel horizontal boundaries and applying vertical loads at its mid-span section.

For the floor slabs illustrated in Fig. 4, there were two tensile-bending loading states: bending about the x-axis and bending about the y-axis. However, only the “bending about the y-axis” scenario was simulated with the high-fidelity slab models. This is because, for the trapezoidal, dovetail, and reentrant composite slabs, their bending resistance about the steel decks' longitudinal direction (x-axis in Fig. 4) could be neglected, which caused by two reasons. First, limited by the weak clip connections between curled sheet edges and the corrugated cross-section geometry, the tensile forces of the profiled steel decks along their transverse direction (y-axis in Fig. 4) could be ignored [50]. Secondly, due to the corrugated cross-section geometry, the composite slabs did not have bottom transverse bars. Hence, the designed trapezoidal, dovetail, and reentrant composite slabs could only develop bending resistance about their y-axis. For the RC slab and rebar-truss composite slab, they could develop bending resistance about both the x-axis and y-axis, as they had two layers of rebars in both directions. For the RC slab, its flexural behavior about the x-axis and y-axis was similar. While for the rebar-truss composite slab, its flexural behavior about the x-axis could be seen as similar to that of the RC slab, since they both had two layers of Φ 8 transverse bars with a spacing of 200 mm and the steel decks cannot develop tensile force along the y-axis. In view of the above, only the “bending about y-axis” scenario was simulated for these floor slabs with the high-fidelity models.

The concrete, steel decks, and bars were modeled by solid elements, shell elements, and beam elements, respectively. The element size of these elements was 25 mm. The bars were perfectly bonded to surrounding concrete, and the relative slips between them were neglected. A friction coefficient of 0.5 was adopted in the surface-to-surface contact between steel decks and concrete [40]. For the rebar-truss composite slab model, the spot welding between rebar-trusses and steel decks was modeled by a spotweld material (MAT100) in LS-DYNA. According to the GB50018–2016 code [51], the shear capacity of each spot welding was 3 kN. As mentioned above, to achieve the tensile-bending loading state, all the degrees of freedom of the element nodes at the longitudinal boundaries parallel to the y-axis were fully restrained, while vertical displacement loading was applied to the middle section of the slab models (Fig. 4).

It is worth mentioning that the high-fidelity modeling method used in this section was validated by Wang et al. [40] based on a composite floor test [25], and more detailed information about the modeling techniques and validation basis can be seen in Reference [40]. The material properties shown in Fig. 5 were used for the high-fidelity slab models. The material properties of profiled steel decks and bars were obtained by standard coupon tests, and the test responses are shown in Fig. 5a. The cylindrical compressive strength of the concrete was 26

MPa. The plastic and softening behavior of concrete were calibrated based on the experiments conducted by Sinha et al. [52] and Gopalratnam et al. [53], and the calibrated response curve of the concrete is given in Fig. 5b.

3.2. Simulation results and discussion

The applied load versus mid-section vertical displacement curves of these high-fidelity slab models are shown in Fig. 4. The ultimate resistance ($F_{u,crb}$, $F_{u,hrb}$) along with the corresponding vertical displacement ($\delta_{u,crb}$, $\delta_{u,hrb}$) and the steel deck fracture displacement (δ_{df}) are listed in Table 1. The flattened *sheet length* of the profiled steel decks and *rebar area* within one-meter width of the floor slab are also listed in Table 1. Due to the corrugated geometry cross section, the *sheet lengths* of the trapezoidal, dovetail, and reentrant profiled steel decks were all larger than one meter. In contrast, the *sheet length* of the rebar-truss profiled steel deck was equal to one meter.

3.2.1. Effect of rebar type

According to the response curves in Fig. 4, the effects of rebar types on the structural behavior are pronounced. As shown by the $F_{u,hrb} / F_{u,crb}$ ratio, except for the trapezoidal composite slabs, all the slab resistance was improved at least by 51% by replacing the CRB550 with HRB400. For the trapezoidal composite slabs with CRB550 or HRB400, all the longitudinal rebars were fractured before the ultimate resistance was reached. After the cross-sectional failure of the longitudinal rebars (displacement = 450 mm), the slab resistance was merely provided by the steel decks, and the load-displacement curves became similar. Consequently, the ultimate resistance of these two trapezoidal composite slabs was approximately equal. The highest $F_{u,hrb} / F_{u,crb}$ ratio was seen in the RC slabs, which was 211%. This was attributed to the fact that a more evident tensile membrane action was developed for the case with HRB400 compared with that with CRB550. In particular, all the longitudinal CRB550 rebars of the RC slab were fractured prior to the displacement reaching 200 mm, whereas this displacement was up to 450 mm for the case with HRB400, ensuring sufficient tensile action of the slab. For the rebar-truss composite slabs, the CRB550 bottom chords fractured at a displacement of 80 mm; in contrast, the fracture of the HRB400 rebar-trusses occurred when the displacement reached 429 mm. This resulted in the slab resistance of the rebar-truss composite slab with HRB400 being significantly higher than that with CRB550 in the range of displacements between 80 mm and 429 mm. When the displacement was greater than 429 mm, the load-displacement curves of these two rebar-truss composite slab models behaved similarly because the slab resistance was mainly provided by the profiled steel decks at this stage. Due to the similar cross-sectional geometry, the structural performance of dovetail and reentrant composite slabs was almost the same, and the $F_{u,hrb} / F_{u,crb}$ ratios of these two slabs were also approximately equal.

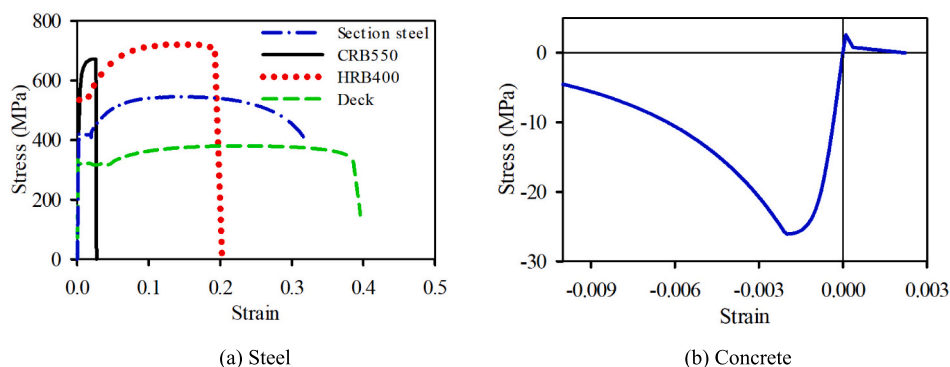


Fig. 5. Material properties.

Table 1
Simulation results of high-fidelity slab models.

Slab type	sheet length (mm/m)	rebar area (mm ² /m)	CRB550			HRB400			$F_{u,hrb} / F_{u,crb}$
			$\delta_{u,crb}$ (mm)	δ_{df} (mm)	$F_{u,crb}$ (kN)	$\delta_{u,hrb}$ (mm)	δ_{df} (mm)	$F_{u,hrb}$ (kN)	
Trapezoidal	1133	251	613	613	1166	573	573	1225	105%
Dovetail	1610	251	332	332	1055	446	446	1599	151%
Reentrant	1660	251	298	298	1026	406	406	1559	152%
Rebar-Truss	1000	895	592	592	1312	429	658	2159	165%
RC	–	502	20	–	324	452	–	686	211%

3.2.2. Effect of different profiled steel decks

In addition to the rebar types, the cross-sectional geometry of the profiled steel decks could also greatly influence the structural behavior of these slab models.

The steel decks' cross-sectional geometry could significantly affect the δ_{df} . As shown in Table 1, the δ_{df} of the dovetail and reentrant composite slabs were smaller than that of the trapezoidal and rebar-truss composite slabs. The relatively early fracture of the dovetail and reentrant profiled steel decks was due to the plastic strain concentration developed at the cross-section where longitudinal rebars fractured, and this strain concentration was caused by the relatively high level of composite action between steel decks and overlaying concrete in these two types of composite slabs. For the dovetail and reentrant steel decks, attributed to the significant gripping forces developed between the concrete and the inverted triangular ribs of the steel decks, the relative sliding between them was effectively prevented. While for the trapezoidal and rebar-truss composite slabs, the friction between the concrete and the steel decks was not as pronounced as that of the dovetail and reentrant composite slabs. This can be explained by Fig. 6, which shows the steel decks' plastic strain contours of the composite slabs with CRB550 at a displacement of 320 mm. Since the longitudinal CRB550 rebars were all fractured before the displacement reached 200 mm, the slab resistance was mainly provided by the steel decks in the loading condition shown in Fig. 6. The relatively strong composite action developed in the dovetail and reentrant composite slabs resulted in a plastic strain concentration of the steel decks at the cross sections where rebar fractured (Fig. 6), which eventually led to the premature fracture of the steel decks at these locations. Although the dovetail and reentrant composite slabs exhibited similar structural behavior, the relatively stronger gripping force between the closed inverted triangles of reentrant steel decks and concrete made the δ_{df} of the reentrant composite slab slightly smaller than that of the dovetail composite slab. On the contrary, relatively low strain concentrations within steel decks were observed in the trapezoidal and rebar-truss composite slabs (Fig. 6), which made these steel decks fractured at relatively large displacements. However, due to the corrugated cross-sectional shape and the tension-bending loading state, a certain degree of strain concentration was

still developed at the trapezoidal steel decks' upper surfaces adjacent to the restrained horizontal boundaries (Fig. 6), which led to the slightly earlier fracture of the steel decks at these locations and also limited the development of the tensile membrane forces. Similar behavior was also observed for the composite slabs with HRB400. Due to the relatively late fracture of the HRB400 rebars, the steel decks' fracture caused by the strain concentration at the rebar failure location was also postponed in the dovetail and reentrant composite slabs.

The steel decks' cross-sectional geometry could also affect the development of the composite slabs' ultimate resistance. The magnitude of the vertical resistance provided by the tensile membrane action was not only related to the in-plane tension (i.e., related to the unit sheet length of the steel decks and the unit rebar area of the longitudinal rebars), but also related to the angle between the in-plane tension and the vertical direction (i.e., related to the vertical displacement). As mentioned above, due to the early fracture of CRB550 rebars, the ultimate resistance of composite slabs with CRB550 was primarily provided by the tensile membrane action of the steel decks. As shown in Table 1, even though the unit sheet lengths of trapezoidal and rebar-truss steel decks were much lower than that of the dovetail and reentrant steel decks, the $F_{u,crb}$ of the trapezoidal and rebar-truss composite slabs were all higher than that of the dovetail and reentrant composite slabs, which was benefited from the relatively larger δ_{df} of the trapezoidal and rebar-truss steel decks. However, for the composite slabs with HRB400, as the steel decks' fracture in the dovetail and reentrant composite slabs was postponed, the vertical resistance provided by the tensile membrane action of these two steel decks was significantly increased. This resulted in both the $F_{u,crb}$ of the dovetail and reentrant composite slabs with HRB400 being larger than that of the trapezoidal composite slabs with HRB400. Regardless of whether CRB550 or HRB400 was used, the rebar-truss composite slab had the highest ultimate resistance among all the floor slabs, while the RC slab had the lowest ultimate resistance.

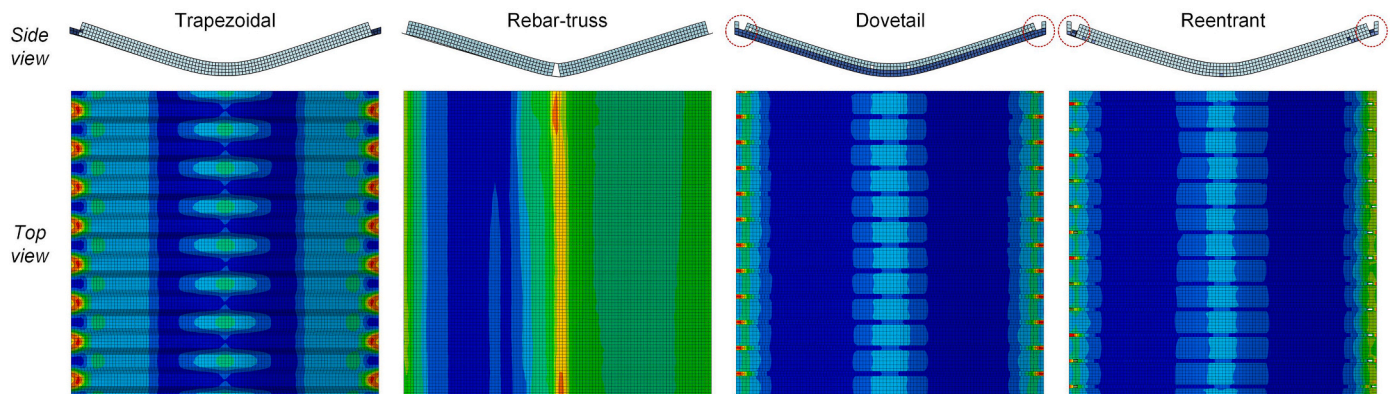


Fig. 6. Steel deck plastic strain development of slabs with CRB550 at a displacement of 320 mm.

4. Reduced-order models of prototype buildings

4.1. Overview and steel frames

An overview of the reduced-order model of a steel frame building is shown in Fig. 7. In particular, the columns, girders, and beams were modeled by the Hughes-Liu beam elements with sectional integration [54], which integration rule used in this study is illustrated in Fig. 7. The material properties used for the columns, girders, and beams are shown as the “Section steel” in Fig. 5, which is the same as that used in the girder flanges of the test specimen conducted by Wang et al. [40]. The welded flanges and web bolts at the connections between floor beams and columns were modeled by discrete beam elements, which load-deformation behavior was simulated with a nonlinear spring (i.e., No. 119 material in LS-DYNA [54]). The axial load-deformation curves used for these spring elements are illustrated in Fig. 8. These springs were assumed to deteriorate after the deformation increased beyond the defined threshold under tension, whereas elastic-plastic behavior without deterioration was assumed under compressive actions. The parameters of the connection springs were calibrated by Wang et al. [11] based on the corresponding high-fidelity models and are listed in Table 2. The vertical shear load at the connection was assumed to be carried by the shear tab only, which vertical shear capacity was calculated according to the GB 50017–2017 [41]. The shear capacity of each bolt spring of the girder-to-column connection and the beam-to-column connection was 235 kN and 91 kN, respectively. The web springs would be deleted when either the axial fracture displacement (δ_0 , Table 2) or the vertical shear force was reached, while the flange springs would be deleted when the axial fracture displacement (δ_0) was reached. The deformations of the connection springs along the other directions were fully restrained. Shear studs were modeled by Hughes-Liu beam elements, which material properties were described in Section 2. As the connection between slabs and floor beams was designed as fully composite, the failure of the shear stud was not simulated. The shear studs were connected to the floor beams through rigid bars.

4.2. Floor slabs

The floor slabs were discretized by 300×300 mm shell elements. The detailed reduced-order modeling schemes for the floor slabs used in the prototype buildings are illustrated in Fig. 9. The concrete, rebars, and steel decks were represented by different integration points in the shell element, and these materials were all simulated by the “MAT-Concrete_EC2” material in LS-DYNA [54], which could simulate plain

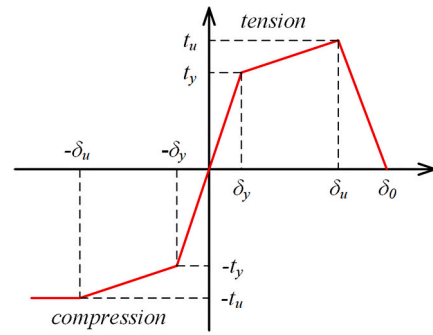


Fig. 8. Axial load-deformation relationship for the connection springs.

Table 2
Calibrated connection spring parameters.

Connection	Spring	δ_y (mm)	t_y (kN)	δ_u (mm)	t_u (kN)	δ_0 (mm)
Girder-to-column	Flange spring	0.02	1354	2.05	1818	2.55
	Bolt spring	1.5	280	20	340	39
Beam-to-column & Beam-to-girder	Flange spring	0.02	571	2	760	2.5
	Bolt spring	1	125	13.5	160	16

concrete, rebars, and reinforced concrete by altering the reinforcement ratio. The Belytschko-Wong-Chiang element formulation incorporated with Flanagan-Belytschko stiffness form hourglass property was used for the slab shell element [54].

4.2.1. RC slab

For the RC slab shell elements, as shown in Fig. 9a, ten integration points were used (i.e., six for concrete and 4 for rebars). Note that the longitudinal and transverse rebars were modeled by separated integration points, which could prevent the fracture of rebars in one direction from causing premature fracture of rebars in the other direction. The thickness of each rebar layer was calculated by dividing the cross-sectional area of single rebar by the rebar spacing.

4.2.2. Trapezoidal composite slab

To simulate the variation of the cross-sectional height of the

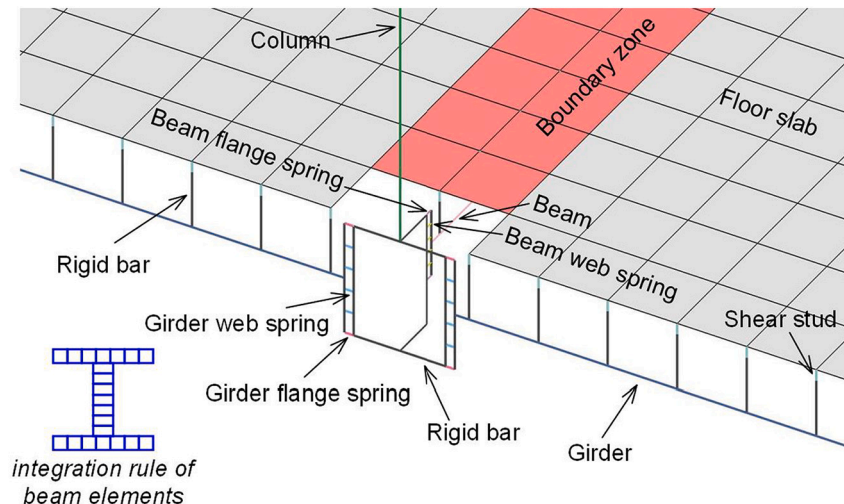


Fig. 7. Modeling details of the connection region.

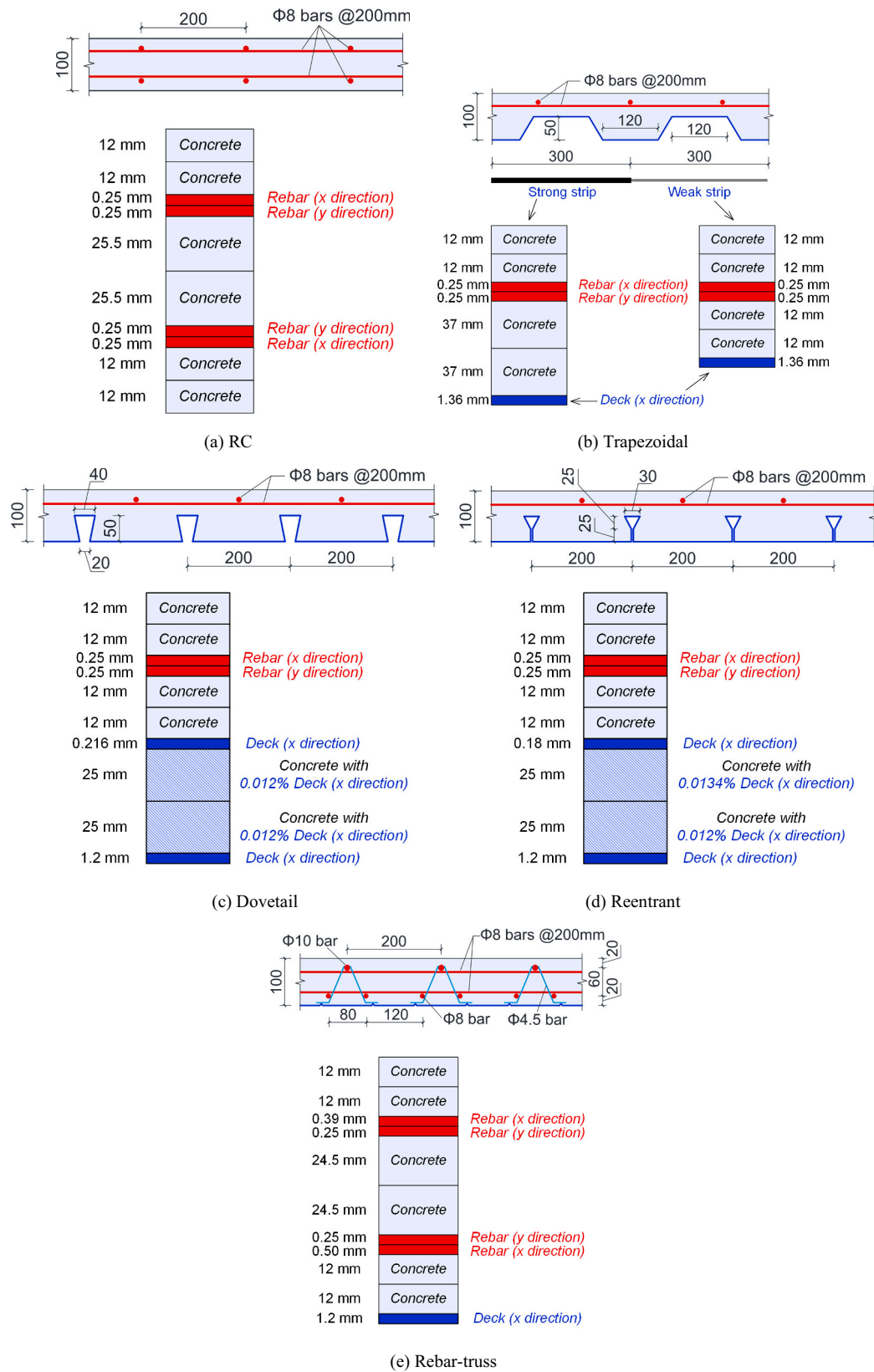


Fig. 9. Reduced-order modeling of floor slabs.

trapezoidal composite slab, two different thickness shell elements (i.e., strong strip and weak strip) were used to model the slab ribs and slab flanges, respectively. As shown in Fig. 9b, the thicknesses of the strong strip and weak strip were 100 and 50 mm, respectively. Each shell

element was composed of four concrete integration points, two rebar integration points, and one steel deck integration element. In the steel deck integration point, the steel decks' resistance along the y-axis direction was neglected, and only its resistance along the x-axis direction

was considered. Due to the corrugated cross-sectional geometry of the trapezoidal composite slabs, within the unit width of the floor slab, the flattened transverse length of the trapezoidal steel decks should be larger than the slab width. In view of this, the corresponding thickness of the steel deck integration point was set as its equivalent thickness, which was calculated as follows: the steel deck thickness (1.2 mm) multiplied by the ratio of the unit *sheet length* (1133 mm, Table 1) to the unit slab width (1000 mm). The value of this equivalent steel deck thickness was 1.36 mm.

4.2.3. Dovetail and reentrant composite slabs

For the dovetail and reentrant composite slabs, as shown in Fig. 9c and d, a total of ten integration points were used to model the shell elements for these slabs. Since the bottom surfaces of these slabs were flat, the thickness of the steel deck layer was set at the original deck thickness, i.e., 1.2 mm. Due to the significant gripping forces between the inverted triangular deck ribs and concrete, these deck ribs were seen as the rebars embedded in the concrete. The top surface of deck ribs was modeled by a separate steel deck layer, which thickness was calculated by multiplying the original deck thickness (1.2 mm) by the ratio of the deck rib width to the deck rib spacing, and this thickness for the dovetail and reentrant steel decks was 0.216 and 0.18 mm, respectively. The vertical parts of the deck ribs were modeled as smeared rebars in the concrete, and the equivalent reinforcement ratios are marked in Fig. 9c

and d.

4.2.4. Rebar-truss composite slabs

As shown in Fig. 9e, the shell elements for the rebar-truss composite slab were modeled by 11 integration points (i.e., six for the concrete, four for rebars, and one for the steel deck). The web rebars were not considered in the shell element.

4.2.5. Material calibration

As shown in Fig. 10, the material properties for the rebar, the steel deck, and the concrete were calibrated based on a 300 × 300 mm square shell element benchmark model, which dimension was identical to that used in the reduced-order models of the prototype building. First, the material properties in Fig. 5a were used to define the stress-strain behavior of the rebars and steel decks, and the corresponding simulation results were shown in Fig.10 and named “MAT172 (scale 1)”. As shown by the “MAT172 (scale 1)” in Fig. 10, except for the CRB550, the numerically calculated fracture displacements of HRB400 and steel deck were all larger than their corresponding test curves. This is because the deformation capacity of HRB400 and steel deck was much higher than that of CRB550, and significant local necking behavior was observed in the coupon test of HRB400 and steel deck before fracture. However, the large size shell element (300 mm) used here could not accurately simulate the local necking behavior because the local deformation had

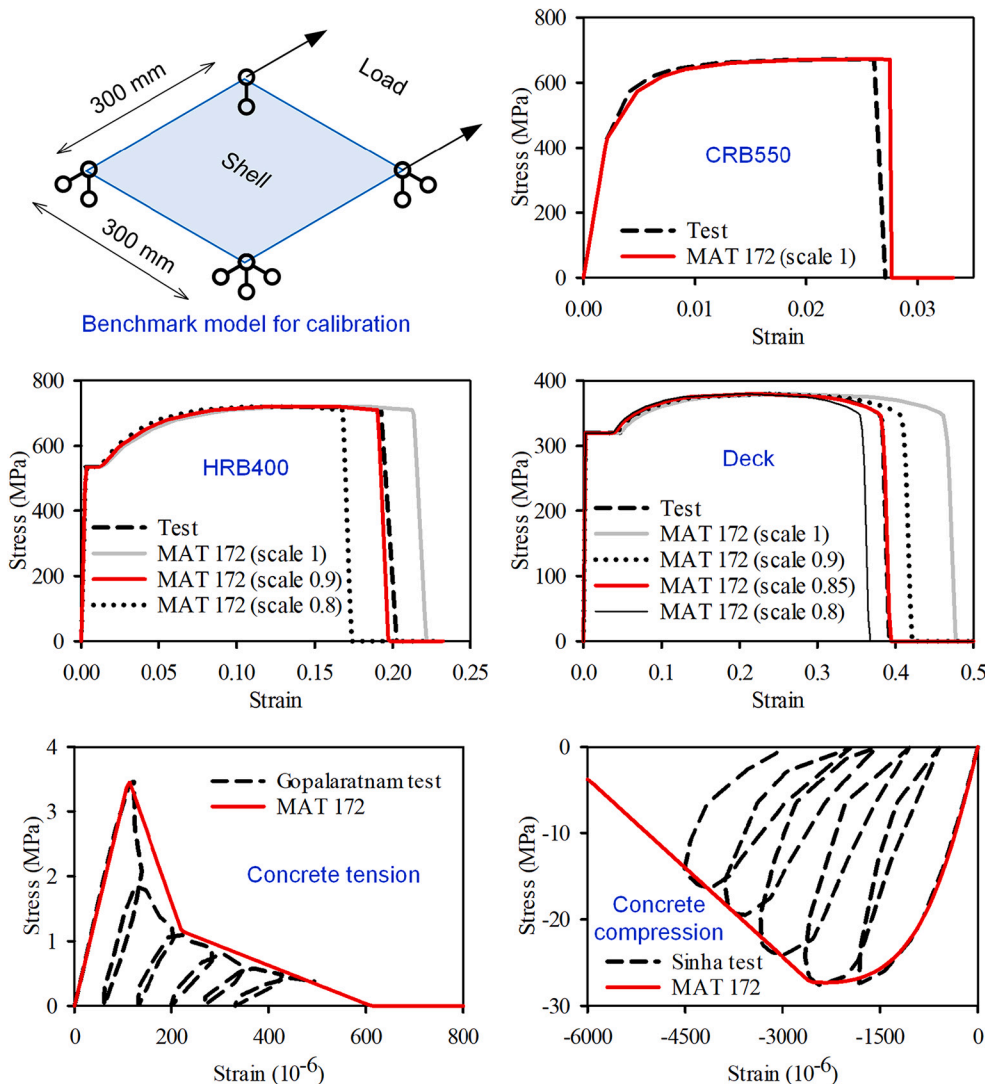


Fig. 10. Material calibrations for the slab shell elements.

been averaged within the element range. To achieve consistency between the test curves and numerical simulations, the corresponding plastic strain values of HRB400 and steel deck were adjusted. As shown in Fig. 10, for HRB400, when the plastic strain was multiplied by a scale factor of 0.9, the numerical result matched its experimental result. For the steel deck, the optimized scale factor was 0.85, and the corresponding fracture strain ϵ_f was 0.33. For the concrete, the Mander concrete model [55] with a confined ratio of 1.05 was adopted to model the concrete behavior. The tests performed by Sinha et al. [52] and Gopalaratnam et al. [53] were used to calibrate the softening properties of concrete under tension and compression. The sufficiency of the calibration can be seen by comparing the test curve and numerical prediction, as shown in Fig. 10.

4.2.6. Calibration of the reduced-order slab models

Based on the modeling detail mentioned above, a reduced-order slab model with a mesh size of 300 mm was built for the 2.4×2.4 m square slab model mentioned in Section 3, and an overview of the model is shown in Fig. 11. Using the calibrated material properties, the bending behavior of different composite slabs about the y-axis was simulated with the reduced-order slab model, and corresponding prediction results were shown in Fig. 4. As shown in Fig. 4, the predictions by the reduced-order models were consistent with that by the corresponding high-fidelity models, except for the dovetail and reentrant composite slabs. While for the dovetail and reentrant composite slabs, the final fracture displacements of the reduced-order models were much larger than that of the corresponding high-fidelity models since the strain concentration phenomenon (Section 3.2.2) of the steel decks was not considered. Therefore, the calibrated steel deck fracture strain was further reduced to consider the effect of the strain concentration in these cases. As shown in Fig. 4, when the steel deck fracture strain was reduced to 0.05, the results of the reduced-order models of the dovetail and reentrant composite slabs matched with that of the corresponding high-fidelity models.

4.3. Deck-to-stud connection

As shown in Fig. 3d, the steel deck edges were connected to the beam top flanges by the shear stud with through-deck welding. Limited by this deck-to-stud connection, the tensile resistance of the steel deck adjacent to this connection cannot be fully developed. Hence, the material properties of the steel deck layer in the shell elements in this region, named as “boundary zone” in Fig. 7, should be modified based on the structural performance of the deck-to-stud connection.

4.3.1. Fracture simulation of profiled steel deck

To characterize the failure of the deck-to-stud connection, the fracture behavior of steel decks needed to be reproduced. As shown in Fig. 12, two types of coupon specimens, flat plate specimen and hole plate specimen, were tested for the steel deck. First, the true stress-strain curve of the steel deck was converted from the corresponding nominal stress-strain curve, and the post-necking relationship of the true stress-

strain curve was determined using the method described by Wang et al. [40]. Then, both flat plate specimen and hole plate specimen were modeled with corresponding quarter models, in which shell element sizes in the core region were 0.5 mm. Based on the test results, the Rice-Tracey fracture model [56] was calibrated as $\epsilon_f = 1.07e^{-1.68\eta}$, where η was stress triaxiality and equal to mean stress divided by von Mises stress. The calibration process can be found in Reference [40]. As shown in Fig. 12b and c, the numerical results of coupon models using the calibrated fracture model matched well with the corresponding experimental results.

4.3.2. Reduced-order modeling approach

As described in Section 2, 38 shear studs were arranged on each beam top flange. Therefore, for the steel decks on each side of the beam, there were 19 shear studs with a spacing of 300 mm, which were labeled as “1 stud”. In addition, the quantity of the shear studs was doubled to investigate the effect of the number of shear studs on the structural robustness, and this case was labeled as “2 studs”. According to the Eurocode [57], the stud spacing parallel to the beam axis should be not less than five times the diameter of the stud, so the stud spacing for the “2 studs” case was chosen as 100 mm. As shown in Fig. 13, two high-fidelity deck-to-stud connection models were modeled with the 0.5 mm size shell elements. The shear studs were completely restrained, while the out-of-plane displacements of the steel decks were fully restrained to simulate the constraint provided by the concrete slab. Lateral tension was uniformly applied to the end edges of the steel decks. As shown in Fig. 13, the strengths of the “1 stud” and “2 studs” cases were about 10 kN and 20 kN, respectively.

As shown in Fig. 14a, a perfectly plastic curve was used to simulate the steel decks at the boundary zone, and the plastic stress of this curve was chosen as the ultimate stress of the steel deck, which was 380 MPa. According to the strength of the deck-to-stud connection mentioned above, the equivalent thicknesses of the bottom steel deck layer (t_e) at the boundary zone were calculated, which were 0.0877 and 0.1754 mm for the “1 stud” and “2 studs” cases, respectively. For the dovetail and reentrant composite slabs, the deck ribs were not considered in the reduced-order models at the boundary zone. The reduced-order modeling scheme for the composite slabs at the boundary zone is illustrated in Fig. 14. Based on the load-displacement curves obtained by the high-fidelity models in Fig. 13, the damage initiation strain and fracture strain of the steel decks at the boundary zone were calibrated, which were 0.09 and 0.10, respectively.

4.4. Constraint, contact, and loading method

Except for the removed column, all column bases were fully restrained. The contact behavior between the slabs and floor beams was modeled by the “Contact Automatic General” algorithm in LS-DYNA. To obtain a more realistic simulation result, the ground was modeled by a rigid wall at the column base level, as illustrated in Fig. 15a. During the simulation, all falling structural parts would fall on the ground simulated by the “rigid wall”.

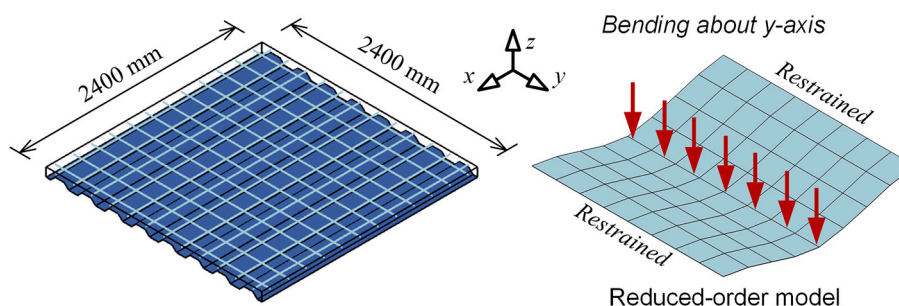
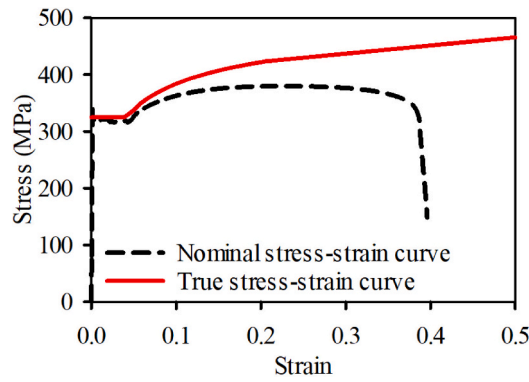
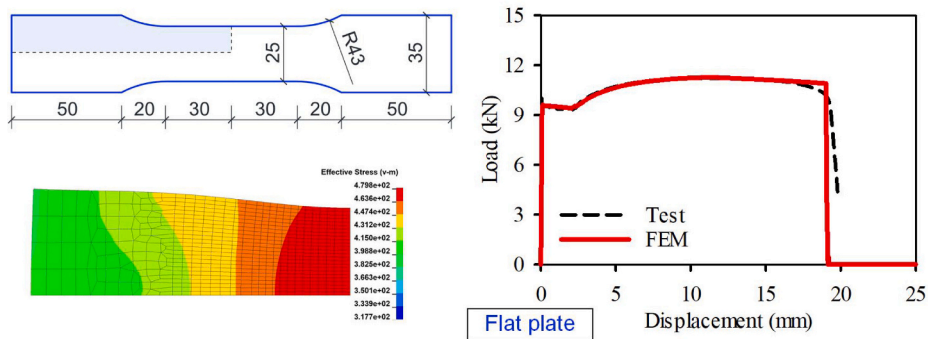


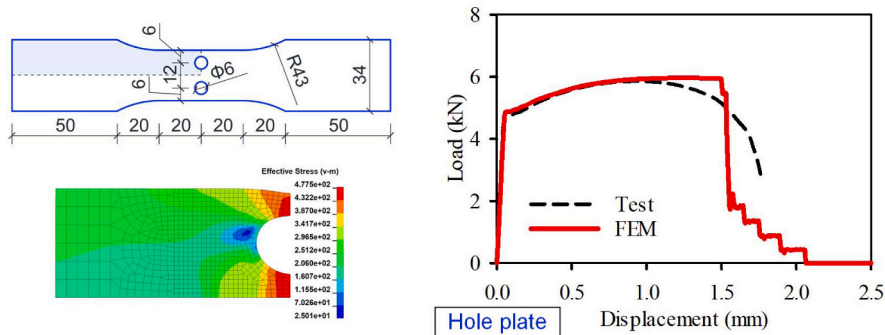
Fig. 11. Calibration of the reduced-order slab model.



(a) True stress -strain curve of steel deck



(b) Flat plate specimen



(c) Hole plate specimen

Fig. 12. Fracture calibration of steel deck.

The loading process of the prototype buildings was divided into two phases. At the 1st phase, a service level gravity load R_d was uniformly applied to all floor slabs of the prototype building. Then, at the 2nd phase, an additional incrementally increasing load was uniformly applied to the affected bays of the removed column until collapse was triggered. The load combination for extraordinary events, $1.2DL + 0.5LL$, in ASCE/SEI 7-16 [58] was chosen as R_d , which was 7 kN/m^2 for the prototype building. All the loading was applied in a pseudo-static manner. As shown in Fig. 3a, given the symmetrical layout of the prototype building, the single-column failure scenarios on the ground floor could be categorized into nine separate cases, coded as follows, A1, A2, A3, B1, B2, B3, C1, C2, and C3. To obtain the relationship between floor load intensity and the vertical displacement of the removed column, the total vertical reaction at the bases of the directly affected columns was exported. However, as shown in Fig. 15a and b, except for the floor areas

of the directly affected bays of the removed column, the directly affected columns also needed to support the floor loadings of the additional tributary area. Considering this issue, the load intensity of the directly affected bays (ω) was calculated by the following equations:

$$\omega = \begin{cases} \frac{\lambda F_c}{nA_a}, & 1^{st} \text{ phase} \\ F_c - \frac{(1-\lambda)F'_c}{nA_a}, & 2^{nd} \text{ phase} \end{cases} \quad (1)$$

$$\lambda = \frac{A}{A_a + A_t} \quad (2)$$

where F_c denoted the total vertical reaction at the bases of the directly affected columns and F'_c referred to the F_c at the dividing point between 1st and 2nd phase. n was the total floor number ($= 5$). A_a stood for the

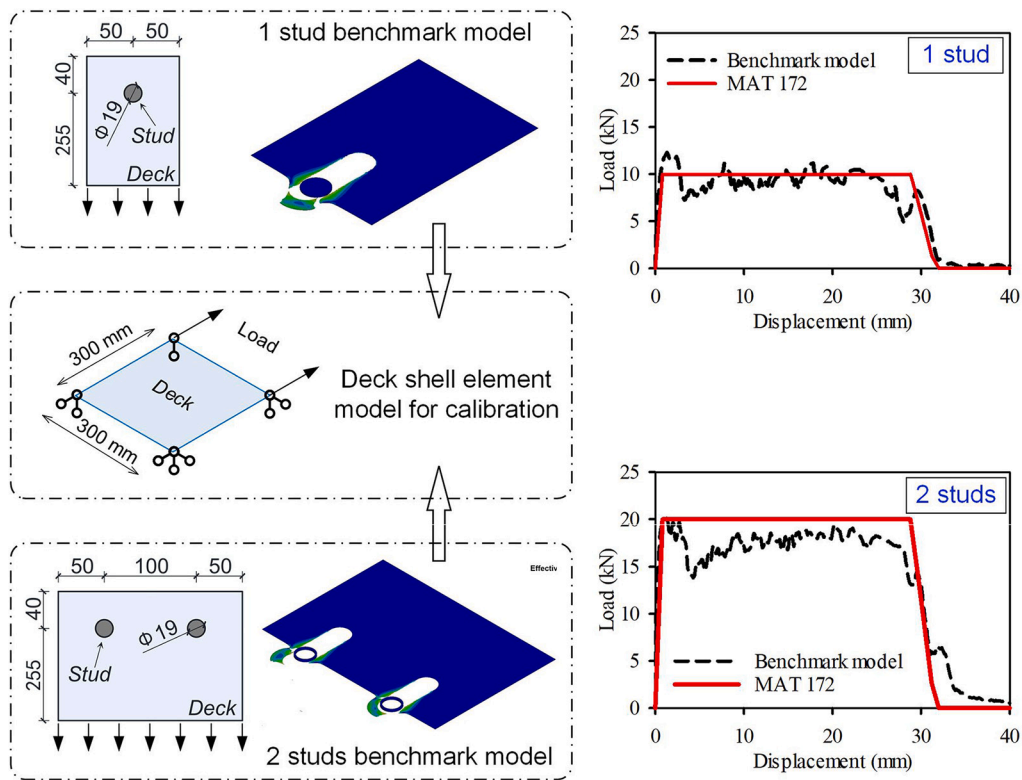


Fig. 13. Reduced-order modeling of the deck-to-stud connection.

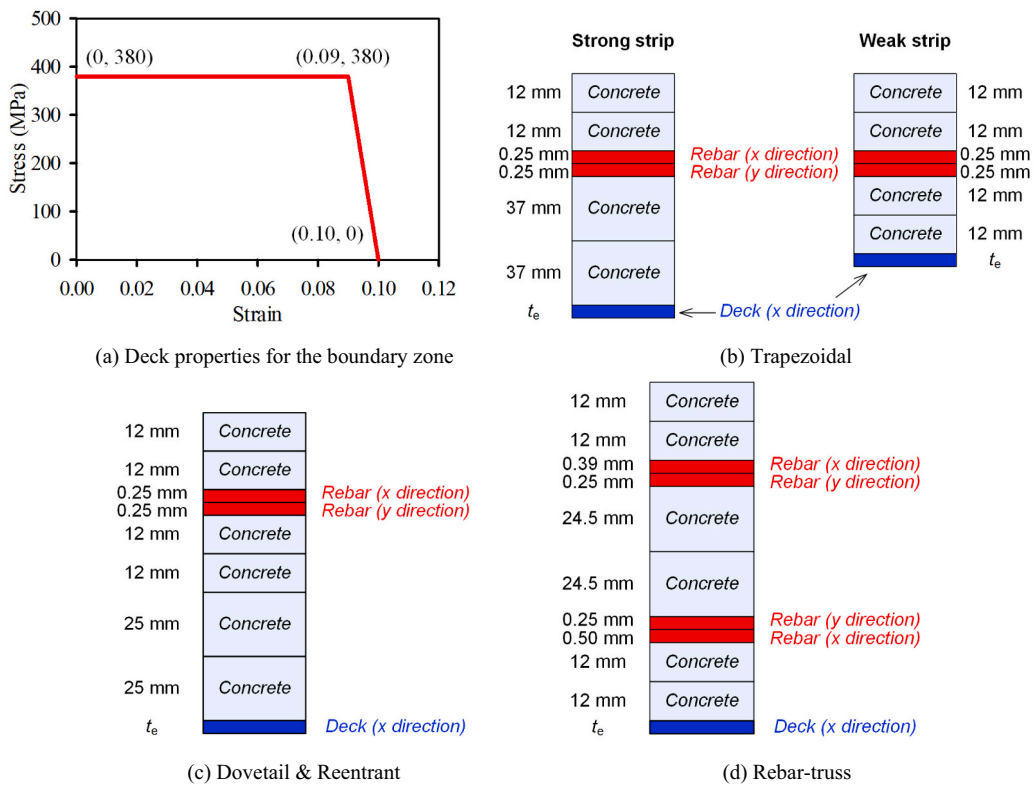
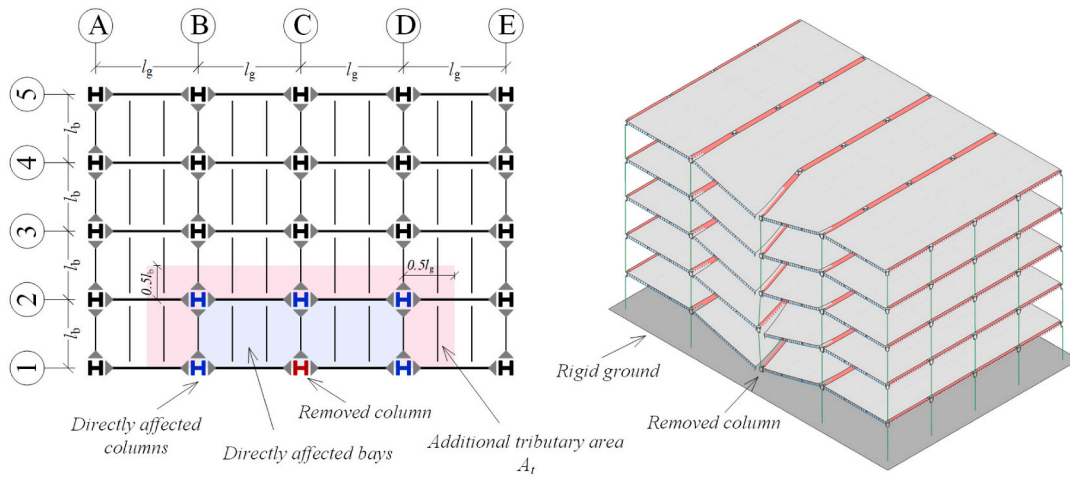


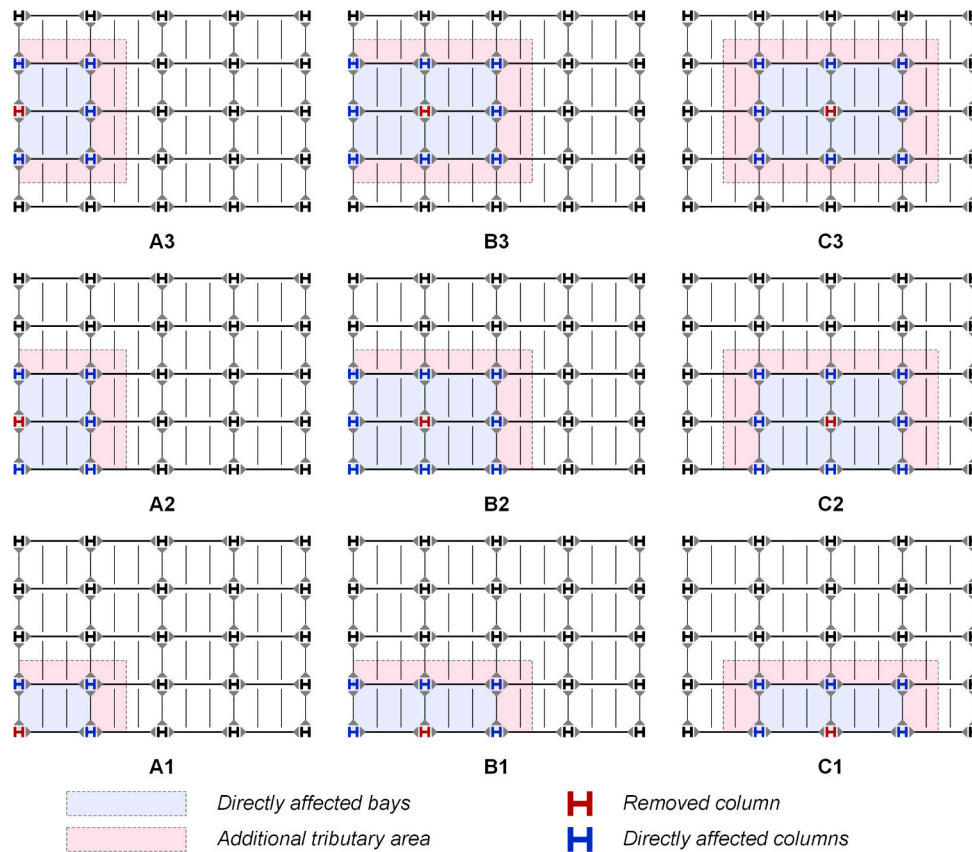
Fig. 14. Reduced-order modeling of the boundary zone.

floor area of the directly affected bays on each floor, while A_t represented the additional tributary area of the directly affected columns on each floor. A_a , A_p , and λ of each column failure scenario are illustrated in

Fig.15b.



(a) Analysis of the prototype building under C1 column failure scenario.



Scenario	A1	A2	A3	B1	B2	B3	C1	C2	C3
λ	4/9	8/15	4/9	8/15	16/25	8/15	4/9	8/15	4/9

(b) Floor area for calculating load intensity under each column failure scenario.

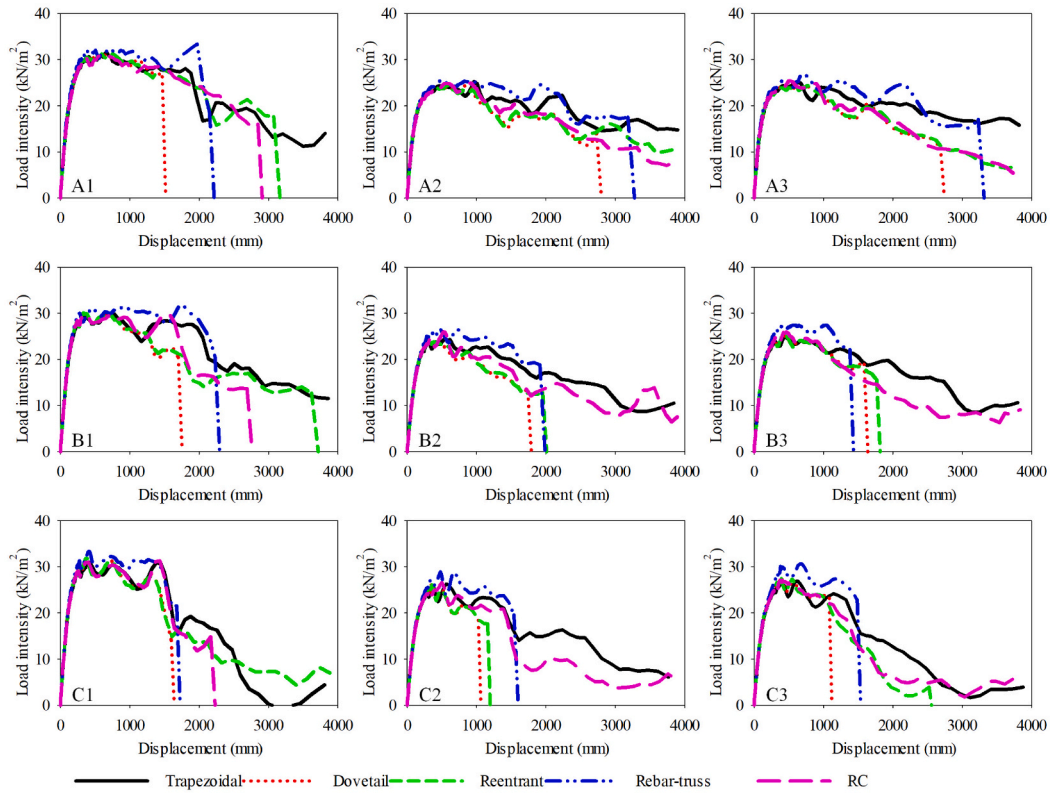
Fig. 15. Analysis method for the prototype building under different column failure scenarios.

5. Robustness evaluation of prototype building and discussion

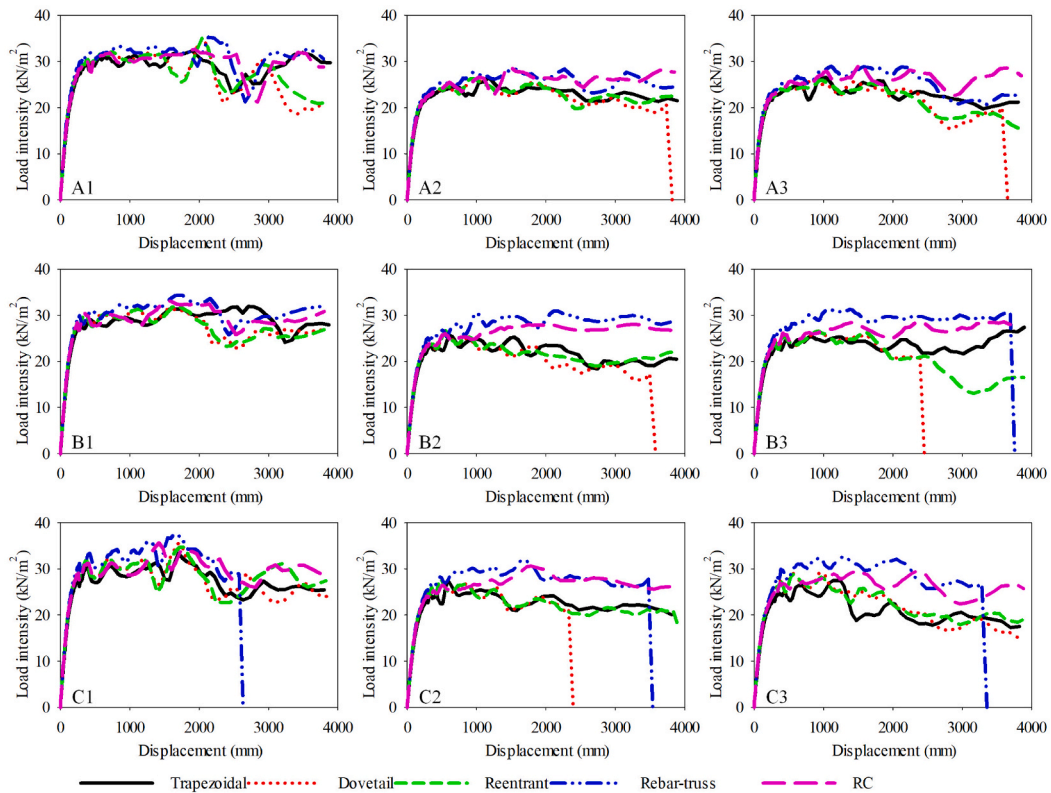
5.1. Analysis of prototype building

With the reduced-order modeling method, the relationship between the load intensity and the vertical displacement at the removed column can be obtained, and the investigated parameters include column failure

location, rebar type, shear stud, steel decks' longitudinal continuity, and floor slab type. The corresponding simulation results are shown in Fig. 16. As mentioned in Section 2, the profiled steel decks' length was 9 m, and they were restrained to the beam top flanges by the shear studs at their longitudinal ends. Thus, in the prototype building described in Section 2, the profiled steel decks were "discontinuous" along their longitudinal direction. In this instance, the shear stud quantity on the

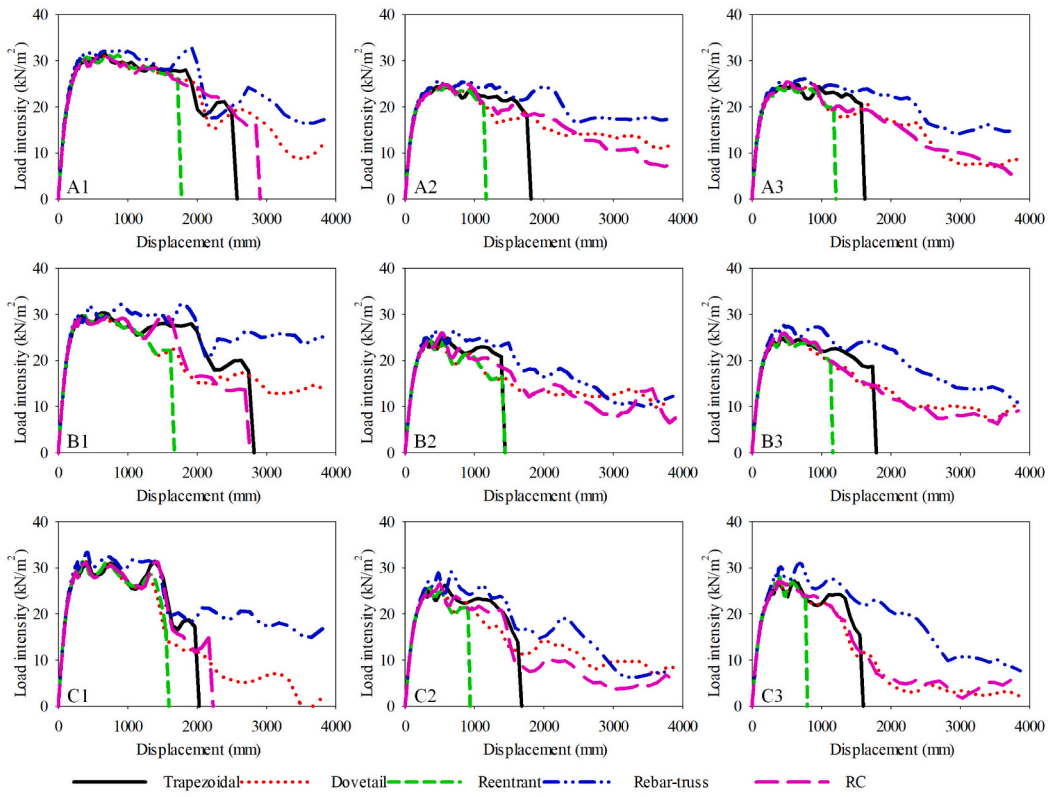


(a) Discontinuous-1stud-CRB550

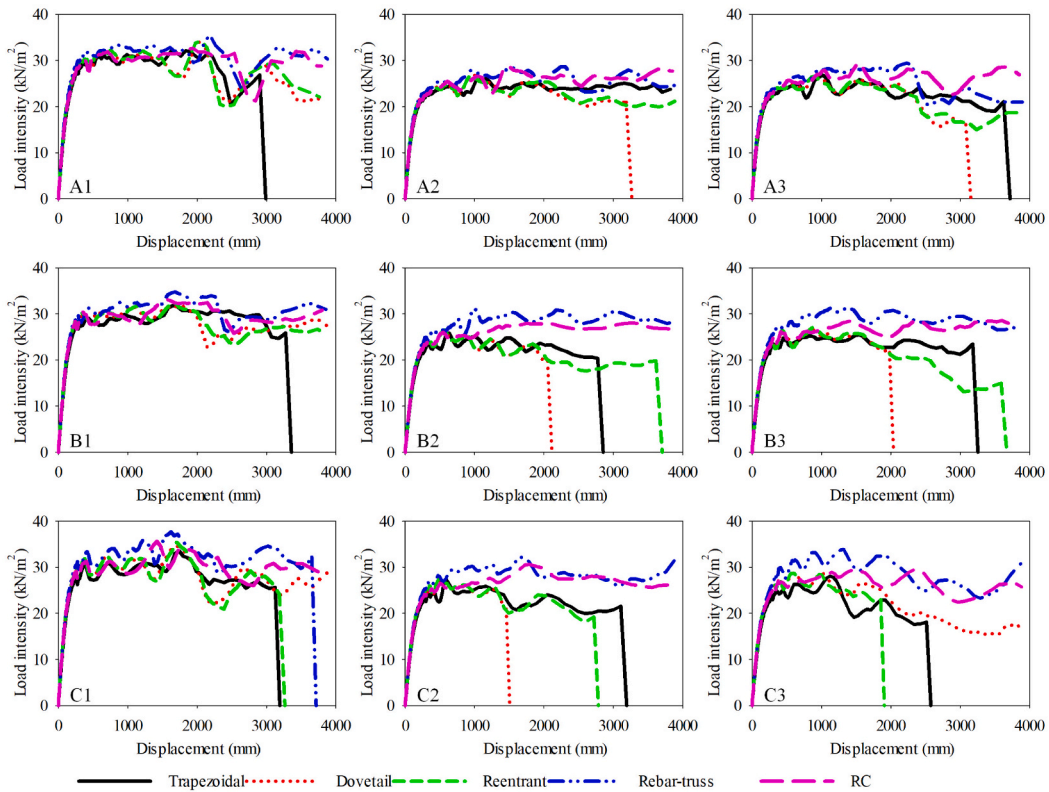


(b) Discontinuous-1stud-HRB400

Fig. 16. Static load intensity – displacement curves of prototype building under different column failure scenarios.

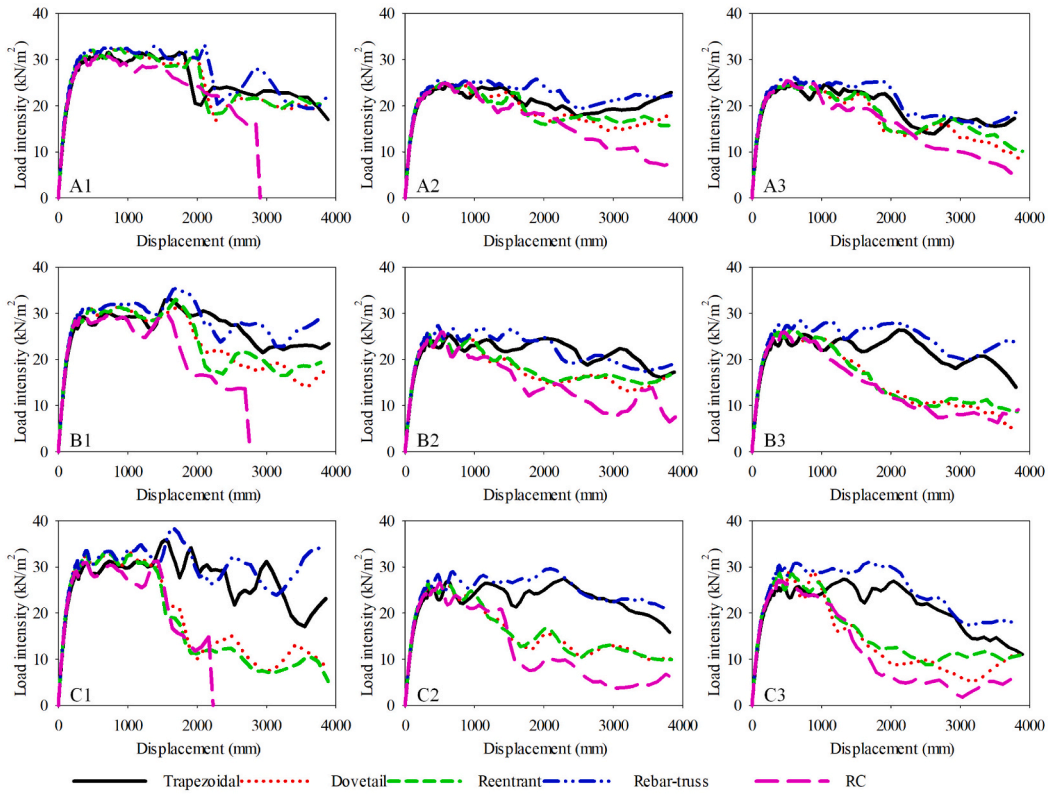


(c) Discontinuous-2stud-CRB550

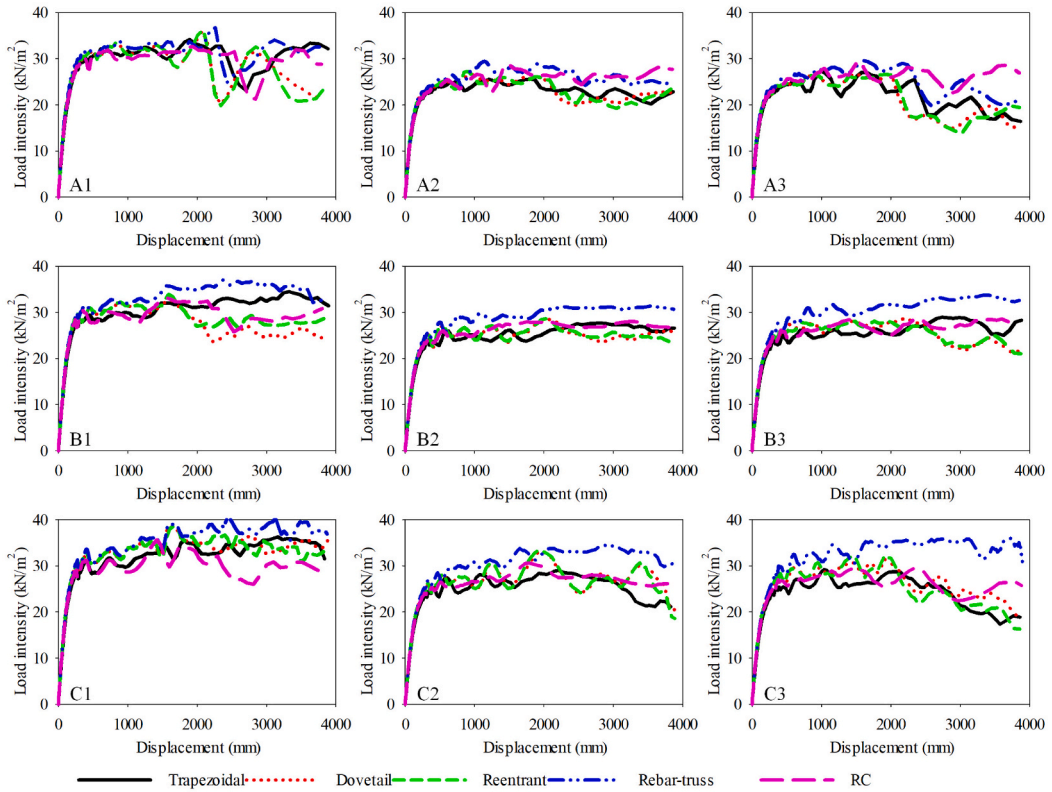


(d) Discontinuous-2stud-HRB400

Fig. 16. (continued).



(e) Continuous-1stud-CRB550



(f) Continuous-1stud-HRB400

Fig. 16. (continued).

beam top flange would affect the development of the steel decks' in-plane tensile membrane force along its longitudinal direction. Given this, the cases with shear stud quantity on each beam top flange of 38 and 76 were analyzed, and for consistency with Section 4.3, these two cases were named as “1 stud” and “2 studs”, respectively. In addition, to further investigate the effect of the longitudinal continuity of the profiled steel decks, the steel decks were ideally assumed to be “continuous” over the entire longitudinal range of the floor slab, as this is the case where the longitudinal continuity was strongest. For this “continuous” case, the shear stud quantity on each beam top flange was 38, identical to the “1 stud” case mentioned above. For comparison purposes, the prototype building with RC floor slabs was also analyzed, and the shear stud quantity was unchanged and consistent with Section 2.

According to the static response curves in Fig. 16, in each simulation scenario, the load-carrying capacity of A1, B1, and C1 cases were significantly higher than the other six cases. This is because, in these three cases, the floor area of the “directly affected bays” needed to be supported by each girder was only half of that of the other six cases [11]. For the prototype building using CRB550 rebars, the load-carrying capacity of the prototype building showed a downward trend after its peak value was reached (Fig. 16a). However, when the CRB550 was replaced by HRB400, the load-carrying capacity of the prototype building would remain at a relatively stable plateau after reaching the peak value (Fig. 16b), which benefitted from the relatively large deformation capacity of HRB400.

When other conditions were the same, the load-carrying capacity of the prototype building with rebar-truss composite slab was higher than that with the other four types of floor slabs (Fig. 16c). This was because the reinforcement ratio of the rebar-truss composite slab was significantly higher than that of the other four types of floor slabs. The rebar-truss composite slab not only had more longitudinal rebars, but also two layers of transverse rebars, while other composite slabs had only one layer of transverse rebars. Hence, like the RC slab, the rebar-truss composite slab could develop flexural resistance about its both strong and weak axes. For the other three types of composite slabs, they could only develop the flexural resistance about their strong axes, while in their weak axis direction, they could only develop the tensile membrane force by the single layer transverse rebars. Besides, as noted in Section 3.2.2, owing to the flat bottom surface, the rebar-truss steel decks had the slightest strain concentration among all the composite slabs, which also enabled the steel decks to develop more tensile membrane action to enhance the overall building's load-carrying capacity.

In the cases of “discontinuous” and using CRB550 (Fig. 16a and c), the load-carrying capacity of the prototype building with RC slab was comparable to those with the trapezoidal, dovetail, or reentrant composite slabs. However, while CRB550 was replaced by HRB400 (Fig. 16b and d), the load-carrying capacity of the prototype building with RC slab became stronger than those with these three composite slabs, and only weaker than that with rebar-truss composite slab. This was because the RC slab had two layers of longitudinal and transverse rebars, and it could develop flexural resistance about its both strong and weak axes. When HRB400 was used, the bi-directional load-carrying mechanism of the RC slab was further enhanced. While for the trapezoidal, dovetail, and reentrant composite slabs, they only had one layer of rebars in these two directions. Moreover, due to the weak resistance of the deck-to-stud connection, the steel decks could not fully develop tensile membrane force, which further limited the development of the overall load-carrying capacity.

Comparing “discontinuous-1stud-CRB550 (Fig. 16a)” and “continuous-1stud-CRB550 (Fig. 16e)”, the load-carrying capacity of the prototype building with trapezoidal or rebar-truss composite slabs was significantly improved under the “continuous” condition, on the contrary, no significant improvement was observed for the prototype buildings with the dovetail and reentrant composite slabs. This was because the premature fracture of CRB550 caused the premature fracture of the dovetail and reentrant steel decks (Section 3.2.2).

After replacing CRB550 with HRB400, i.e., “continuous-1stud-HRB400 (Fig. 16f)”, the fracture of the dovetail and reentrant steel decks were postponed attributed to the relatively late fracture of HRB400; thus, the load-carrying capacity of prototype buildings with these two steel decks was significantly enhanced and was comparable to that with trapezoidal steel decks.

5.2. Robustness evaluation method

Note that the above-mentioned analysis was conducted in a static manner, which could not fully represent the actual performance of the prototype building under dynamic conditions. Therefore, based on the energy-based method proposed by Izzuddin et al. [59], the nonlinear static response can be converted into an equivalent dynamic response. As shown in Fig. 17, this energy-based method assumes the external work done by gravity loads is all converted into the internal energy of the structure. At a certain displacement, the dynamic resistance is equal to the static curve's integrated area divided by this displacement. After reaching the static ultimate capacity (F_{su}), the load-carrying capacity of the structure will become unstable, which may suddenly break down [60,61]. In this context, the displacement corresponding to F_{su} is regarded as the termination point of the equivalent dynamic response curve. Prior to this termination point, the dynamic ultimate capacity (F_{du}) achieved by the equivalent dynamic response curve can be regarded as the structure's ultimate capacity against progressive collapse. The minimum F_{du} of all column loss scenarios is regarded as the ultimate capacity of the objective structure. The progressive collapse resistance demand of this structure is chosen as the load combination for extraordinary events R_d , which is specified in ASCE/SEI 7-16 [58]. The ratio of “minimum F_{du} ” to “ R_d ” is regarded as the structural robustness index Ω . If Ω is larger than 1, this structure is considered to be robust enough to avoid progressive collapse. Otherwise, it is necessary to select an appropriate structural robustness enhancement method to redesign and re-evaluate the objective structure until its ultimate capacity is higher than its progressive collapse resistance demand.

5.3. Robustness evaluation and discussion

Using the energy-based method depicted in Fig. 17, the dynamic ultimate capacity of the above-mentioned nonlinear static pushdown analyses is obtained, which is listed in Table 3. As shown in Table 3, the lowest Ω occurred in the cases of “discontinuous-1stud-CRB550” with dovetail and reentrant composite slab, which value was 232%. This indicated that all the prototype buildings simulated in this study had sufficient structural robustness in preventing disproportionate collapse induced by single ground floor column failure. The greatest Ω value was 342%, which was observed in the case of “discontinuous-2stud-HRB400” with the rebar-truss composite slab.

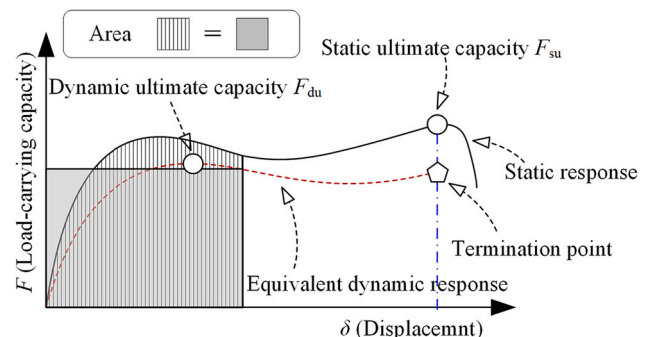


Fig. 17. Equivalent dynamic response.

Table 3
Dynamic ultimate resistance F_{du} of prototype building.

Rebar	Column Loss Location	Discontinuous								Continuous				RC
		1 stud				2 studs				1 stud				
		Trapezoidal	Devotail	Reentrant	RebarTruss	Trapezoidal	Devotail	Reentrant	RebarTruss	Trapezoidal	Devotail	Reentrant	RebarTruss	
CRB550	A1	25.4	25.4	26.4	29.2	25.6	26.0	25.9	29.2	25.8	27.4	27.6	30.1	24.9
	A2	21.4	21.2	20.0	19.9	19.1	20.1	20.0	19.5	19.9	20.3	20.2	23.4	21.5
	A3	20.8	21.1	21.1	22.0	20.5	21.4	20.2	22.1	20.4	21.5	21.5	21.4	19.9
	B1	25.2	20.9	21.0	28.3	24.8	24.4	21.1	27.0	27.3	28.3	28.4	29.6	26.4
	B2	19.4	16.3	16.3	20.0	20.1	17.5	17.7	21.8	19.8	17.5	17.5	20.0	19.6
	B3	18.9	18.6	18.9	22.0	18.6	18.8	19.2	20.3	22.6	21.3	21.1	22.9	19.5
	C1	23.1	23.1	22.8	24.2	27.0	22.9	22.9	24.2	28.6	27.3	24.1	30.9	27.0
	C2	20.3	18.3	18.3	20.9	20.5	17.9	18.2	22.4	23.5	17.9	17.8	25.8	20.1
	C3	21.5	19.4	19.3	23.8	21.3	19.4	19.5	24.0	23.1	21.7	19.8	27.3	19.1
	Min	18.9	16.3	16.3	19.9	18.6	17.5	17.7	19.5	19.8	17.5	17.5	20.0	19.1
Max	25.4	25.4	26.4	29.2	27.0	26.0	25.9	29.2	28.6	28.3	28.4	30.9	27.0	
Min / R_d (Ω)		270%	232%	232%	284%	266%	250%	252%	279%	283%	251%	249%	286%	272%
Max / R_d		363%	364%	377%	418%	386%	371%	371%	417%	408%	404%	406%	442%	385%
HRB400	A1	28.5	29.0	28.8	30.5	28.1	28.7	29.0	30.6	29.4	29.9	30.0	31.1	29.1
	A2	21.9	21.8	21.8	24.4	21.6	22.1	21.8	25.3	23.1	22.2	22.0	23.7	23.1
	A3	21.9	21.7	22.0	23.9	21.9	22.1	22.0	26.0	22.1	24.0	23.9	25.1	24.3
	B1	28.5	28.0	27.9	29.6	27.1	28.4	28.2	29.6	30.0	28.8	28.9	31.8	27.7
	B2	19.5	20.0	19.9	26.6	19.7	20.1	20.2	23.9	24.3	24.4	24.3	28.5	25.6
	B3	23.3	21.9	22.0	26.6	22.7	22.1	21.9	26.6	24.6	25.6	25.4	29.7	25.2
	C1	27.7	28.6	28.8	31.0	28.0	28.8	28.8	31.1	31.5	31.0	31.2	33.7	28.3
	C2	20.2	20.1	20.2	26.9	20.1	20.7	20.2	26.9	25.0	26.0	26.0	29.9	25.2
	C3	22.9	24.0	21.8	27.5	22.9	24.0	21.6	28.0	23.3	27.1	27.2	32.3	26.1
	Min	19.5	20.0	19.9	23.9	19.7	20.1	20.2	23.9	22.1	22.2	22.0	23.7	23.1
Max	28.5	29.0	28.8	31.0	28.1	28.8	29.0	31.1	31.5	31.0	31.2	33.7	29.1	
Min / R_d (Ω)		279%	286%	284%	341%	282%	288%	288%	342%	316%	317%	314%	338%	330%
Max / R_d		408%	414%	412%	443%	402%	412%	414%	444%	449%	442%	446%	481%	415%

*Notes: the unit of the F_{du} in this table is kN/m^2 .

5.3.1. Effect of rebar type

According to the analysis results in Table 3, after replacing CRB550 with HRB400, the Ω for all cases was improved. However, the Ω for the prototype buildings with trapezoidal composite slabs had the least improvement, and the corresponding improvement ratios in “discontinuous-1stud”, “discontinuous-2stud”, and “continuous-1stud” cases were 3%, 6%, and 11%, respectively. While for the prototype buildings with dovetail, reentrant, rebar-truss, and RC slabs, Ω was considerably improved with HRB400. The insensitivity of the prototype building with the trapezoidal composite slab to the rebar type's alteration could be explained by Fig. 4 and Table 1. As noted in Section 3, regardless of whether CRB550 or HRB400 was used, the ultimate resistance of the trapezoidal composite slab was achieved after the fracture of the longitudinal rebars, and was approximately equal, as it was primarily provided by the trapezoidal steel decks. While for the RC slab, its load-carrying capacity was mainly dependent on rebars. Similarly, due to the high reinforcement ratio, the resistance of rebar-truss composite slab would also be highly affected by the rebars. Since the steel decks' fracture behavior in the dovetail and reentrant composite slab was seriously affected by the rebars' deformability, the prototype buildings with these two slabs would be greatly influenced by the rebar type.

5.3.2. Effect of the continuity of profiled steel decks

By comparing the Ω of “discontinuous-1stud” and “discontinuous-2stud” cases, it can be seen that increasing the shear stud quantity on the beam flange had a neglected effect on improving the structural robustness. This was because the capacity of the deck-to-stud connection was low compared to the tensile capacity of the steel deck net section, so increasing its quantity did not have a considerable effect on the overall load-carrying capacity. While comparing the Ω of “discontinuous-1stud” and “continuous-1stud” cases, for the prototype buildings with trapezoidal, dovetail, or reentrant composite slabs and using CRB550, the structural robustness could be improved at least by 5% after increasing the steel decks' longitudinal continuity; for those using HRB400, this enhanced percentage would be at least 11%. However, for the prototype buildings with rebar-truss composite slabs, the structural robustness had not been improved after using “continuous” steel decks. As shown in Table 3, the minimum F_{du} in the “continuous-1stud” with rebar-truss composite slab cases was achieved by the B2 and A2 column loss scenarios for the prototype buildings using CRB550 and HRB400, respectively. In these two column loss scenarios, the floor slab failure was primarily governed by the failure of the rebars in the transverse direction; hence, increasing the longitudinal continuity of the steel decks had a negligible effect on the structural robustness of the prototype buildings with the rebar-truss composite slab. It would be concluded that merely improving the steel decks' longitudinal continuity had a limited effect on the structural robustness, and if the steel decks' transverse continuity could be improved simultaneously, it might have a more noticeable improvement on the structural robustness.

5.3.3. Effect of different profiled steel decks

For the “discontinuous-1stud-CRB550” cases, the lowest Ω was obtained from the prototype buildings with dovetail and reentrant composite slabs, which was 232%, and was 86%, 82%, and 85% of those with trapezoidal, rebar-truss and RC slabs, respectively. As mentioned above, when using CRB550, due to the strain concentration, dovetail and reentrant steel decks were fractured much earlier than the trapezoidal and rebar-truss steel decks. This made the prototype buildings with these two slabs had a relatively lower structural robustness value. After replacing CRB550 with HRB400, i.e., “discontinuous-1stud-HRB400”, attributed to the good deformation capacity of HRB400, the steel deck fracture of the dovetail and reentrant composite slabs was significantly delayed; thus, the Ω of the prototype buildings with these two slabs was effectively improved; and the lowest Ω was obtained from the prototype building with the trapezoidal composite slab. For the prototype building designed in Section 2, regardless of whether CRB550

and HRB400 were used, the highest Ω was achieved when the rebar-truss composite slab was used, followed by the RC slab. This benefited from the bi-directional load-carrying mechanism in these two slabs. In contrast, the trapezoidal, dovetail, and reentrant composite slabs behaved as one-way slabs, which limited their structural robustness. Hence, when using the trapezoidal, dovetail, and reentrant steel decks, it would be necessary to enhance their transverse continuity to improve their bi-directional load-carrying mechanism.

6. Conclusions

This study presented a novel reduced-order modeling method to analyze the structural performance of steel frame buildings with different floor slabs under column loss scenarios. This modeling method was verified by the relatively high-fidelity models, which were verified by the full-scale composite floor test and detailed material coupon tests. This reduced-order modeling method was applied to the progressive collapse simulation of a five-story prototype building. Based on this building, the effect of different floor slabs and different slab rebars on its structural robustness was investigated. Finally, based on the simulation results, the following conclusions are reached:

1. For the prototype building with floor slabs using CRB550, the minimum dynamic ultimate capacity was at least 132% higher than the corresponding R_d . While for the prototype building with floor slabs using HRB400, this improvement ratio was 179%.
2. Attributed to the steel decks and additional bottom layer rebars, the minimum dynamic ultimate capacity of the prototype building with rebar-truss composite slab was higher than that with the RC slab or other composite slabs.
3. The structural robustness of the prototype building with RC slab was better than that with trapezoidal, dovetail, and reentrant composite slabs because they lacked bottom transverse slab rebars.
4. Owing to the similar cross-sectional configuration, the structural behavior of the dovetail and reentrant composite slabs was almost identical, and the structural robustness of the prototype buildings with these two composite slabs was also similar.
5. After increasing the steel decks' longitudinal continuity, the minimum dynamic ultimate capacity of the prototype buildings with trapezoidal, dovetail, and reentrant composite slabs was all improved. However, for the prototype building with the rebar-truss composite slab, the improvement of the steel decks' longitudinal continuity had a negligible effect on its minimum dynamic ultimate capacity.

CRedit authorship contribution statement

Junjie Wang: Conceptualization, Methodology, Investigation, Writing – original draft. **Ke Ke:** Software, Supervision, Resources, Funding acquisition, Writing – review & editing. **Wei Wang:** Resources, Supervision, Writing – review & editing.

Declaration of Competing Interest

There is no financial/personal interest or belief that could affect our objectivity. There are no potential conflicts of interest either.

Acknowledgments

This work is supported by National Natural Science Foundation of China under Grant No. 52178111 and 51890902. The corresponding author is truly thankful for the outpouring love and constant support from his wife Siqin, his 27-month-old daughter Yutong and all his families, particularly during this challenging period.

References

- [1] U. Starossek, *Progressive Collapse of Structures*, Second Edition, ICE Publishing, London, 2017.
- [2] U. Starossek, M. Haberland, Approaches to measures of structural robustness, *Struct. Infrastruct. Eng.* 7 (2011) 625–631.
- [3] DoD, Department of Defense, Design of Buildings to Resist Progressive Collapse: Unified Facilities Criteria UFC 4-023-03. Washington, DC, 2016.
- [4] GSA, General Service Administration, Alternate Path Analysis and Design Guidelines for Progressive Collapse Resistance, Washington, DC, 2013.
- [5] EN 1991-1-7, Eurocode 1: Actions on structures, part 1–7: General actions—Accidental actions, European Committee for Standardization, Brussels, 2006.
- [6] Li H. Modeling, Behavior and Design of Collapse-Resistant Steel Frame Buildings (PhD thesis), University of Michigan, Ann Arbor, MI, 2013.
- [7] F. Sadek, Y. Bao, J.A. Main, H.S. Lew, Evaluation and enhancement of robustness for reinforced concrete buildings, *J. Struct. Eng.* 148 (1) (2022) 04021248.
- [8] H. Qiao, Y. Yang, J. Zhang, Progressive collapse analysis of multistory moment frames with varying mechanisms, *J. Perform. Constr. Facil.* 32 (4) (2018) 04018043.
- [9] F. Di Trapani, G. Tomaselli, L. Cavaleri, G. Bertagnoli, Macroelement model for the progressive-collapse analysis of infilled frames, *J. Struct. Eng.* 147 (6) (2021) 04021079.
- [10] F. Freddi, L. Ciman, N. Tondini, Retrofit of existing steel structures against progressive collapse through roof-truss, *J. Constr. Steel Res.* 188 (2022), 107037.
- [11] J. Wang, W. Wang, Macromodeling approach and robustness enhancement strategies for steel frame buildings with composite slabs against column loss, *J. Struct. Eng.* 148 (2022) 04021238.
- [12] F. Sadek, S. El-Tawil, H.S. Lew, Robustness of composite floor systems with shear connections: modeling, simulation, and evaluation, *J. Struct. Eng.* 134 (2008), 1717–1125.
- [13] Y. Alashker, S. El-Tawil, F. Sadek, Progressive collapse resistance of steel-concrete composite floors, *J. Struct. Eng.* 136 (2010) 1187–1196.
- [14] Y. Alashker, H. Li, S. El-Tawil, Approximations in progressive collapse modeling, *J. Struct. Eng.* 137 (2011) 914–924.
- [15] H. Li, S. El-Tawil, Three-dimensional effects and collapse resistance mechanisms in steel frame buildings, *J. Struct. Eng.* 140 (2014) A4014017.
- [16] L. Guo, S. Gao, F. Fu, Y. Wang, Experimental study and numerical analysis of progressive collapse resistance of composite frames, *J. Constr. Steel Res.* 89 (2013) 236–251.
- [17] B. Yang, K.H. Tan, Behavior of composite beam-column joints in a middle-column-removal scenario: experimental tests, *J. Struct. Eng.* 140 (2014) 04013045.
- [18] E.S. Johnson, J.E. Meissner, L.A. Fahnestock, Experimental behavior of a half-scale steel concrete composite floor system subjected to column removal scenarios, *J. Struct. Eng.* 142 (2015) 04015133.
- [19] W. Wang, J. Wang, X. Sun, Y. Bao, Slab effect of composite subassemblies under a column removal scenario, *J. Constr. Steel Res.* 129 (2017) 141–155.
- [20] M. Hadjoannou, S. Donahue, E.B. Williamson, M.D. Engelhardt, Large-scale experimental tests of composite steel floor systems subjected to column loss scenarios, *J. Struct. Eng.* 144 (2018) 04017184.
- [21] Q.N. Fu, K.H. Tan, X.H. Zhou, B. Yang, Three-dimensional composite floor systems under column-removal scenarios, *J. Struct. Eng.* 144 (2018) 04018196.
- [22] J. Wang, W. Wang, D. Lehman, C. Roeder, Effects of different steel-concrete composite slabs on rigid steel beam-column connection under a column removal scenario, *J. Constr. Steel Res.* 153 (2019) 55–70.
- [23] R. Zandonini, N. Baldassino, F. Freddi, G. Roverso, Steel-concrete frames under the column loss scenario: an experimental study, *J. Constr. Steel Res.* 162 (2019), 105527.
- [24] C.A. Dimopoulos, F. Freddi, T.L. Karavasilis, G. Vasdravellis, Progressive collapse resistance of steel self-centering MRFs including the effects of the composite floor, *Eng. Struct.* 208 (2020), 109923.
- [25] J. Wang, W. Wang, Y. Bao, Full-scale test of a steel–concrete composite floor system with moment-resisting connections under a middle-edge column removal scenario, *J. Struct. Eng.* 146 (2020) 04020067.
- [26] L.M. Ren, B. Yang, K. Chen, Y.J. Sun, D.Y. Kong, Progressive collapse of 3D composite floor systems with rigid connections under external column removal scenarios, *J. Struct. Eng.* 146 (2020) 04020244.
- [27] S.Y. Lee, S.Y. Noh, D. Lee, Comparison of progressive collapse resistance capacities of steel ordinary and intermediate moment frames considering different connection details, *Eng. Struct.* 231 (2021), 111753.
- [28] S.T. Hoffman, L.A. Fahnestock, Behavior of multi-story steel buildings under dynamic column loss scenarios, *Steel Compos. Struct.* 11 (2) (2011) 149–168.
- [29] H. Li, X. Cai, L. Zhang, B. Zhang, W. Wang, Progressive collapse of steel moment-resisting frame subjected to loss of interior column: experimental tests, *Eng. Struct.* 150 (2017) 203–220.
- [30] B.I. Song, H. Sezen, Experimental and analytical progressive collapse assessment of a steel frame building, *Eng. Struct.* 56 (2013) 664–672.
- [31] B.I. Song, K.A. Giriunas, H. Sezen, Progressive collapse testing and analysis of a steel frame building, *J. Constr. Steel Res.* 94 (2014) 76–83.
- [32] B. Yang, K.H. Tan, G. Xiong, S.D. Nie, Experimental study about composite frames under an internal column-removal scenario, *J. Constr. Steel Res.* 121 (2016) 341–351.
- [33] J. Wang, W. Wang, Y. Bao, D. Lehman, Full-scale test of a steel moment-resisting frame with composite floor under a penultimate edge column removal scenario, *J. Constr. Steel Res.* 162 (2019), 105717.
- [34] G. Zhou, J. Shi, P. Li, H. Li, Characteristics of structural state of stress for steel frame in progressive collapse, *J. Constr. Steel Res.* 160 (2019) 444–456.
- [35] A. Astaneh-Asl, E. Madsen, D. McCallen, C. Noble, Study of Catenary Mechanism of Cables and Floor to Prevent Progressive Collapse of Buildings Subjected to Blast Loads, Dept. of Civil and Env. Eng., Univ. of California at Berkeley, California, 2001.
- [36] F. Fu, Progressive collapse analysis of high-rise building with 3-D finite element modeling method, *J. Constr. Steel Res.* 65 (2009) 1269–1278.
- [37] F. Fu, 3-D nonlinear dynamic progressive collapse analysis of multi-storey steel composite frame buildings—parametric study, *Eng. Struct.* 32 (2010) 3974–3980.
- [38] L. Kwasiński, Nonlinear dynamic simulations of progressive collapse for a multistory building, *Eng. Struct.* 32 (2010) 1223–1235.
- [39] Q.N. Fu, K.H. Tan, X.H. Zhou, B. Yang, Numerical simulations on three-dimensional composite structural systems against progressive collapse, *J. Constr. Steel Res.* 135 (2017) 125–136.
- [40] J. Wang, W. Wang, X. Qian, Progressive collapse simulation of the steel-concrete composite floor system considering ductile fracture of steel, *Eng. Struct.* 200 (2019), 109701.
- [41] Ministry of Housing and Urban-Rural Development of the People's Republic of China, GB50017–2017. Standard for Design of Steel Structures, China Planning Press, 2017.
- [42] Ministry of Housing and Urban-Rural Development of the People's Republic of China, GB50011–2010. Code for Seismic Design of Buildings, China Building Industry Press, 2016.
- [43] Ministry of Housing and Urban-Rural Development of the People's Republic of China, GB50009–2012. Load Code for Design of Buildings, China Building Industry Press, 2012.
- [44] China Association for Engineering Construction Standardization, CECS 273: 2010. Code for Composite Slabs Design and Construction, China Building Industry Press, 2010.
- [45] Ministry of Housing and Urban-Rural Development of the People's Republic of China, GB50010–2010. Code of Design of Concrete Structures, China Building Industry Press, 2015.
- [46] W. Li, Q. Yang, L. Qian, Design of truss deck concrete slab, *Build. Struct.* 36 (2006) 87–89.
- [47] China Steel New Material Technology Co. Ltd. <https://www.zoogo.net>.
- [48] J.W. Rackham, G.H. Couchman, S.J. Hicks, Metal Cladding & Roofing Manufacturers Association, Steel Construction Institute (Great Britain). Composite slabs and beams using steel decking: Best practice for design and construction. Wirral, Cheshire: Metal Cladding and Roofing Manufacturers Association, in partnership with the Steel Construction Institute, 2009.
- [49] GB/T 10433–2002, Cheese Head Studs for Arc Stud Welding, General Administration of Quality Supervision, Inspection and Quarantine of the People's Republic of China, Beijing, 2002.
- [50] T.W. Francisco, Structural Integrity of the Composite Slab in Steel Gravity Framing Systems (PhD thesis), Purdue University, West Lafayette, IN, 2014.
- [51] Ministry of Housing and Urban-Rural Development of the People's Republic of China, Technical Code of Cold-Formed Thin-Wall Steel Structures, China Planning Press, Beijing, 2016.
- [52] B.P. Sinha, K.H. Gerstle, L.G. Tulin, Stress-strain relations for concrete under cyclic loading, *J. Proc.* 61 (2) (1964) 195–212.
- [53] V.S. Gopalratnam, S.P. Shah, Softening response of plain concrete in direct tension, *J. Proc.* 82 (3) (1985) 310–323.
- [54] LS-DYNA R11, Keyword User's Manual, LiverMore Software Technology, California, 2018.
- [55] J.B. Mander, M.J.N. Priestley, R. Park, Theoretical stress-strain model for confined concrete, *J. Struct. Eng.* 114 (1988) 1804–1826.
- [56] J.R. Rice, D.M. Tracey, On the ductile enlargement of voids in triaxial stress fields, *J. Mech. Phys. Solids.* 17 (1969) 201–217.
- [57] EN 1994-1-1, Eurocode 4: Design of Composite Steel and Concrete Structures—Part 1–1: General Rules and Rules for Buildings, European Committee for Standardization, Brussels, 2009.
- [58] ASCE/SEI 7–16, Minimum Design Loads and Associated Criteria for Buildings and Other Structures (ASCE Standard - ASCE/SEI 7–16), American Society of Civil Engineers, Reston, Virginia, 2017.
- [59] B.A. Izzuddin, A.G. Vlassis, A.Y. Elghazouli, D.A. Nethercot, Progressive collapse of multi-storey buildings due to sudden column loss—Part I: Simplified assessment framework, *Eng. Struct.* 30 (2008) 1308–1318.
- [60] Y.H. Bao, J.A. Main, S.Y. Noh, Evaluation of structural robustness against column loss: methodology and application to RC frame buildings, *J. Struct. Eng.* 143 (2017) 04017066.
- [61] J.A. Main, Composite floor systems under column loss: collapse resistance and tie force requirements, *J. Struct. Eng.* 140 (2014) A4014003.